Sedmá studentská vědecká konference fyziky pevných látek a materiálů
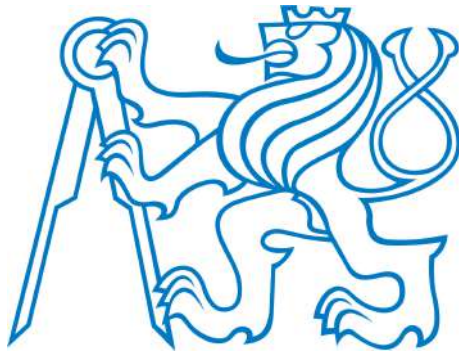

18. – 22. 9. 2017
Sedliště

České vysoké učení technické v Praze
Fakulta jaderná a fyzikálně inženýrská
Katedra inženýrství pevných látek

Děkujeme sponzorovi!

Vážení a milí čtenáři.

Dostává se vám do ruky - již posedmé - sborník příspěvků naší studentské vědecké konference pořádané každoročně Katedrou inženýrství pevných látek Fakulty jaderné a fyzikálně inženýrské Českého vysokého učení technického v Praze s podporou Studentského grantového systému ČVUT. V roce 2017 se konference konala pod názvem Sedmá studentská vědecká konference fyziky pevných látek a materiálů (SVK FPLM 7). Jak název napovídá, rozšířili jsme obsah konference o témata zaměřená na nauku o materiálech, abychom umožnili - i přes omezení rozsahu finanční podpory ze strany SGS - plnohodnotně prezentovat výsledky výzkumné činnosti i studentům partnerské Katedry materiálů.

Sedmý ročník konference se konal ve stejném místě jako ročník loňský, tedy v penzionu Zahrádka v obci Sedliště u Nepomuku, v zářijovém termínu 18. - 22. 9. 2017. Zde je třeba velmi poděkovat majiteli penzionu, panu Stanislavu Šelmátovi, který pouze pro nás otevřel penzion na dobu konání konference, a dále pracovníkům penzionu, kteří se podíleli na vytvoření bezchybně fungujícího ubytovacího a stravovacího zázemí akce.

Na konferenci bylo prezentováno 37 příspěvků, z toho 21 studentských a 16 lektorských přednesených zvanými hosty. Hlavní tématický „záběr"konference byl letos volně navázán na odbornou činnost Multi-disciplinárního centra pokročilých materiálů AdMat (https://admat.fjfi.cvut.cz/ admatwiki/doku.php) podpořeného projektem 14-36566G Grantové agentury České republiky pro centra excelentního základního výzkumu. Kromě uvedené série přednášek byl důležitou součástí SVK FPLM 7 i program doprovodný, v rámci kterého proběhl večerní workshop zaměřený na praktickou demonstraci možností a postupů 3D tisku, a dále pak dvě exkurze: v Atomovém muzeu Javor 51 nacházejícím se poblíž obce Míšov (viz http://www.atommuzeum.cz) a v muzeu rallye legend Škoda (pro obrazovou dokumentaci viz https://skoda-virt.cz/cz/fotogalerie/vystavy-automobilu/456-expozice-rallylegendy-skoda/5314).

Příspěvky byly věnovány výzkumu široké škály problémů z oborů fyziky biomaterálů, polymerů, termoelektrik, kovových slitin, funkčních materiálů a multiferroik, studovaných prostřednictvím rozmanitých metod experimentální a teoretické charakterizace jejich morfologie, reálné krystalové struktury, mechanických, optických, elektrických a magnetických vlastností. Tradičně vysoká formální i

věcná stránka příspěvků podnítila řadu živých diskuzí, které představují jednu ze základních ingrediencí našich SVK. Texty studentských příspěvků jsou shromážděny v tomto sborníku, rozšířené texty vybraných prací pak budou publikovány, podobně jako v loňském roce (viz https://ojs.cvut.cz/ojs/index.php/APP/issue/view/600) v recenzovaném časopise Acta Polytechnica CTU Proceedings.

Jako každoročně končím své úvodní slovo poděkováním: Děkuji mým partnerům z organizačního výboru - Martinovi Drábovi, Tomáši Koubskému a Petrovi Sedlákovi - za výbornou spolupráci, jejímž výsledkem byl bezchybný a hladký průběh konference, všem účastníkům z řad pracovníků KIPL a externím lektorům za jejich kvalitní příspěvky a čas, který přípravě svých prezentací věnovali, a především všem studentským účastníkům za jejich pečlivou výzkumnou práci a tvůrčí entuziasmus, který je nadějí nejen pro další rozvoj fyziky pevných látek a materiálových věd, ale i obecné vzdělanosti v našich zemích.

SVK FPLM 7 je úspěšně za námi, pokochejme se obsahem shromážděných příspěvků a těšme se na další pokračování v roce 2018!

Za kolektiv organizátorů

Ladislav Kalvoda, vedoucí KIPL FJFI ČVUT v Praze

Ionized Jet Deposition System

Jakub Skočdopole

Department of Solid State Engineering, Faculty of Nuclear Sciences and Physical
Engineering, Czech Technical University in Prague
jakub.skoc@gmail.com

Abstract

Ionized jet deposition (IJD) is very flexible method for thin film deposition, which
uses pulsed electron beam. The method is capable of deposition dielectric, metals,
compounds as high temperature superconductors and even polymers. The flexibility
of IJD is not only in the variety of deposition materials, but also in the adjustable
parameters during deposition. IJD is excellent choice as laboratory deposition system.

Keywords: Thin film; Ionized Jet Deposition.

Introduction

IJD is Physical Vapor deposition method for preparation of thin films. IJD uses a pulsed
electron beam to ablate the target material. The biggest advantage of IJD is flexibility.
The method is capable of deposition various materials as dielectrics, metals, compounds
and polymers without any major changes in the settings. The electron pulse has enough
energy to ablate the target material with no differences, thus it conserves the stoichiometry
of target material, which is often crucial parameter. Furthermore the plasma created
from ablation has temperature hundreds of degree Celsius. This fact enables the system
to deposited organic materials. The flexibility of the system is also in the adjustable
parameters of deposition. These parameters are distance between target and substrate,
substrate, acceleration potential, frequency of pulses, temperature of substrate, deposition
time, working gas and working gas pressure.

Theory

The IJD working tool is a pulsed energetic electron beam. The beam is generated in the
IJD source. The main part of the IJD source is a hollow flight-through cathode. An
electron discharge trigger is attached to the cathode and serves as controller of the main
discharge and for the generation of the dense electron pulse directed towards the target.
The main cathode electrode has the form of a hollow cylinder with openings in both
bases. The hollow cathode produces, owing to a Hollow cathode effect, a dense bunch of
energetic electrons[1], that leave the hollow cathode towards the target in the final stage
of the process. The electrons then create a conductive channel by ionizating the working
gas, which is blown trough the IJD source toward the target. The created plasma channel
has not enough capacity to transfer all electrons in one time, thus is created potential
differences inside the plasma channel called double layer. The double layer provides to the
electrons additional energy to ablate the material. The electrons of the bunch hitting the
target surface interact with the atoms of the target transferring to them their kinetic energy
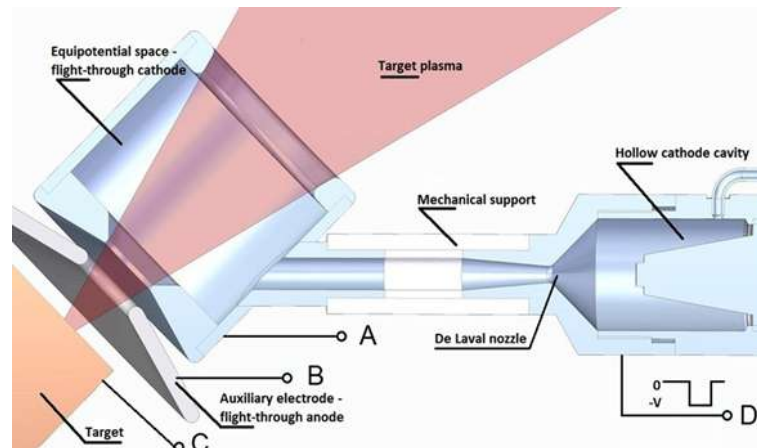and creating a plume of energetic and highly ionized target plasma. The plasma plume

Figure 1: Schematic of IJD source.

which is predominantly expanding in the direction perpendicular to the target surface faces the hollow cathode, enters the smaller opening in the cylinder base facing the target, expands (flies) through the hollow cylinder and leaves the hollow cathode through the larger opening base towards the substrate see Figure 1 [1].

Experiment

Choosing the right deposition parameters have crucial role on the final attributes of the prepared thin film. Here is list of basic parameters and attributes, which mainly depends on them.

- Distance between target and substrate: Morphology of the film.
- Substrate: Adhesion and phases (amorphous, crystalline etc.).
- Acceleration potential: Structure and morphology.
- Frequency of pulses: Speed of deposition.
- Temperature of substrate: Inner structure.
- Deposition time: Thickness.
- Working gas: Reactive or non reactive deposition.
- Working gas pressure: Structure and morphology.

Experimental equipment

In our laboratory at KIPL is the first IJD system in the central Europe named JetDep100.

The system was design to be very easily upgradable. Currently the system has only one IJD source and fixed target and substrate holder. For the next year is planned to extend the system with rotary target holder, which provide more homogeneous ablation of the target and with the rotary-heated sample holder to provide more option to control the structure and homogeneity of the films.

More equipment can be add to the system for example thickness analyser to control the thickness of the film during deposition or second IJD source, which will provide option to deposited more complex multilayer.

Figure 2: IJD system in KIPL laboratory.

Conclusions

The Ionized Jet Deposition is great choice as laboratory system for preparation of thin films. The system JetDep 100 is now fully functional. For more precise control of the deposition process is however necessary to add more equipment.

References

[1] J. Skocdopole. *IJD deposition of ultra-hard thin layers onto substrates of high-alloy steels - an application in medicine study.* Prague. Master thesis. Czech Technical University in Prague. Faculty of Nuclear Science and Physical Engineering, 2017.

Výzkum precipitace v tenkých NiTi vláknech

Ondřej Tyc[1,2], Jan Pilch[2], Petr Šittner[2]

[1]Katedra materiálů, Fakulta jaderná a fyzikálně inženýrská, České vysoké učení technické v Praze

[2]Oddělení funkčních materiálů, Fyzikální ústav, Akademie věd České republiky

tycondre@fjfi.cvut.cz

Abstrakt

Precipitace fáze Ni_4Ti_3 ve slitině NiTi je důležitým procesem, který ovlivňuje superelastické vlastnosti, únavu materiálu a mez pevnosti. V této práci byla použita jedinečná metoda pulsního žíhání elektrickým proudem společně s konvenčním žíháním v peci, což umožnilo oddělit vliv procesů rekrystalizace a zotavení od precipitačního zpevnění. Pomocí precipitace lze kontrolovatelně upravit tvar superelastické hysterezní smyčky a zvýšit mez pevnosti až o 20 %. Avšak vždy dochází ke zkracování transformační deformace superelastického cyklu. Pomocí maloúhlového rozptylu neutronů byla stanovena velikost Ni_4Ti_3 precipitátů. Při žíhání 350 °C/2 h vznikají precipitáty o velikosti cca 10 nm. S rostoucí teplotou žíhání jejich velikost narůstá až na cca 500 nm po žíhání 550 °C/2 h a superelastická křivka již není stabilní při cyklickém zatěžování.

Klíčová slova: NiTi; Pulsní žíhání; Precipitační zpevnění; Superelasticita.

Úvod

Intermetalická slitina NiTi, známá pod komerčním jménem Nitinol, vykazuje jev tvarové paměti a superelastické vlastnosti. Díky tomuto chování našel Nitinol uplatnění v oblastech jako je lékařství, letecký nebo automobilový průmysl [1].

Ve slitině NiTi s nadbytkem niklu jsou známé 3 druhy precipitátů: Ni_4Ti_3, Ni_3Ti_2 a Ni_3Ti. Při precipitaci tak dochází ke snižování koncentrace niklu v matrici, což vede ke snižování transformačních napětí při superelastickém cyklování [2]. Z hlediska aplikací jsou nejdůležitější precipitáty fáze Ni_4Ti_3. Ty mají romboedrickou krystalovou mřížku ($a = 0,6704$ nm, $\alpha = 113,85°$), čočkovitý tvar a nukleují při relativně nízkých teplotách (pod 500 °C) [3]. Malé precipitáty jsou koherentní s matricí a vytváří ve svém okolí pole deformací [4], což zvyšuje mez pevnosti [5] a způsobuje tvorbu R-fáze v NiTi matrici [2].

V tomto výzkumu byla použita unikátní metoda pulsního žíhání elektrickým proudem [6], což umožňuje do určité míry oddělit procesy zotavení a rekrystalizace od precipitačních procesů, které při klasickém žíhání probíhají zároveň. Je tedy možné lépe studovat vliv samotné precipitace na vlastnosti Nitinolu.

Experiment

Experimenty byly provedeny na vláknech o průměru 50 μm, jejichž redukce průřezu při tváření za studena byla 35 % a koncentrace niklu 50,9 at. %. Mez pevnosti v tomto stavu byla 1900 MPa. Nejprve byla vlákna žíhána elektrickým pulsem (50 Wmm^{-3}/50 ms). Pak následovalo precipitační žíhání v peci při teplotách 350, 395, 460 a 520 °C po dobu 2, 5, 15, 30, 60 a 120 min. Nakonec byla vlákna mechanicky testována (superelastické cyklování a tahová zkouška) při teplotě 40 °C. Určení velikosti a objemového podílu precipitátů pomocí maloúhlového rozptylu neutronů (SANS) bylo provedeno ve Švýcarsku v zařízení PSI. Vzorky byly žíhány při teplotách 350, 400, 450, 500, 550, 600, 650 a 900 °C po dobu 2 h.

Výsledky a diskuze

Vývoj superelastických vlastností

Výchozí hodnota horního transformačního napětí po úvodním pulsu byla 685 MPa. Kvůli žíhání dochází vždy přibližně k exponenciálnímu poklesu transformačních napětí v závislosti na čase, jelikož klesá koncentrace Ni v matrici a tvoří se Ni_4Ti_3 precipitáty. Nejvýraznějšího poklesu o 250 MPa bylo dosaženo žíháním 460 °C/1 h. Změny v superelastickém chování bylo možno pozorovat již po dvou minutách žíhání i při teplotě 350 °C, což naznačuje vysokou rychlost precipitace a krátkou nukleační dobu.

Dalším důležitým zjištěním je zkracování transformační deformace po precipitačním žíhání. Pokles byl opět nejvýraznější po žíhání 460 °C/1 h z původní hodnoty 6,8 % na 4,5 %. Důvodem je pokles objemu superelastické NiTi matrice a tvorba precipitátů, které nemají superelastické vlastnosti. Důvodem může být i působení deformačních polí precipitátů a změna v šíření rozhraní mezi austenitem a martenzitem při superelastickém zatěžování.

Stanovení velikosti precipitátů

Značnou výhodou použití metody SANS je určení střední velikosti částic v celém objemu vzorku, ale touto metodou nelze určit jejich složení. Při žíhání 350 °C/2 h došlo ke vzniku Ni_4Ti_3 precipitátů o velikosti okolo 8 nm. Velikost postupně narůstá s rostoucí teplotou. Avšak mezi teplotami 500 °C a 550 °C velikost prudce narůstá z 50 nm na téměř 500 nm. Dále se již velikost příliš nemění. Při teplotě 900 °C dochází k rozpouštění precipitátů a zbývají jen inkluze karbidu TiC, který byl také detekován a bývá běžně přítomen v superelastické NiTi slitině.
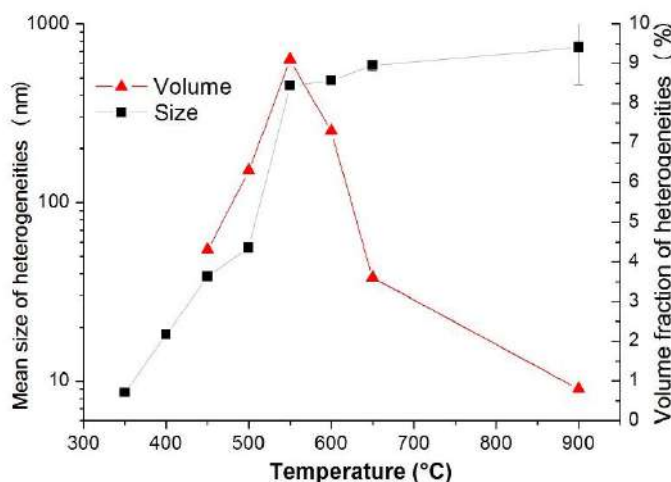
Obrázek 1: Střední velikost a objemový podíl precipitátů (heterogenit) určený metodou SANS.

Vývoj meze pevnosti

V mezi pevnosti, určené z jednotlivých testů, lze pozorovat jednoznačné rozdíly (obr. 2). Při žíhání na teplotách 350 °C a 395 °C dochází pouze k nárůstu meze pevnosti oproti výchozí hodnotě 1430 MPa po úvodním pulsním žíhání, naopak při teplotě 520 °C dochází pouze k poklesu. Malé precipitáty vznikají při nízkých teplotách, jak bylo uvedeno v předchozí sekci, což způsobuje postupný nárůst meze pevnosti až na hodnotu 1680 MPa. Při 460 °C je patrný rychlý nárůst v úvodních fázi následovaný poklesem, který byl pravděpodobně způsoben hrubnutím precipitátů. Při teplotě 520 °C je velikost precipitátů mnohonásobně větší než při nižších teplotách a možná již dochází i k tvorbě další fáze Ni_3Ti_2.
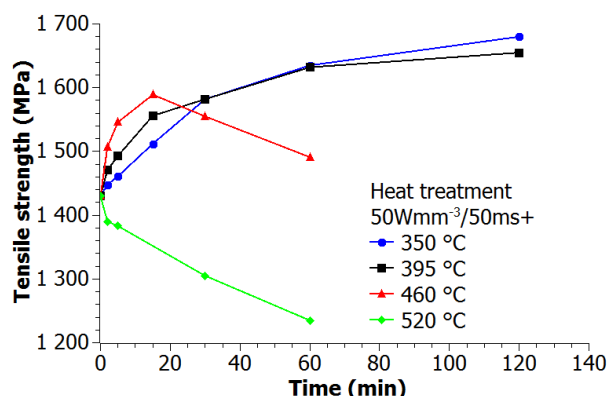
Obrázek 2: Vývoj meze pevnosti v závislosti na čase žíhání při různých teplotách.

Závěr

Výsledky precipitačních experiment lze shrnout do následujících bodů:

- Vytvořením malých (cca 10nm) precipitátů při 350 °C bylo dosaženo nejvyššího nárůstu meze pevnosti (1430 MPa → 1680 MPa) v rámci parametrů experimentu.
- Prudký nárůst velikosti precipitátů mezi 500 °C and 550 °C byl pozorován pomocí metody SANS, což souhlasí s poklesem meze pevnosti a stability superelastických cyklů.
- Pomocí precipitace bylo dosaženo poklesu horního transformačního napětí až o 250 MPa.
- Precipitace výrazně zkracuje délku transformační deformace.

Reference

[1] M. J. Mahtabi, N. Shamsaei, M. R. Mitchell. Fatigue of Nitinol: The state-of-the-art and ongoing challenges. *J Mech Behav Biomed Mater* **50**: 228–254, 2015.

[2] X. Wang, S. Kustov, K. Li, D. Schryvers, B. Verlinden, J. Van Humbeeck. Effect of nanoprecipitates on the transformation behavior and functional properties of a Ti–50.8 at.% Ni alloy with micron-sized grains. *Acta Mater* **82**: 224–233, 2015.

[3] K. Otsuka, C. M. Wayman. Shape Memory Materials. *Cambridge University Press*, Cambridge, 1998.

[4] W. Tirry, D. Schryvers. Quantitative determination of strain fields around Ni_4Ti_3 precipitates in NiTi. *Acta Mater* **53**: 1041-1049, 2005.

[5] A. R. Pelto, J. Dicello, S. Miyazaki. Optimisation of processing and properties of medical grade Nitinol wire. *Min Invas Ther & Allied Technol* **9**: 107-118, 2000.

[6] R. Delville, J. Malard, J. Pilch, P. Sittner, D. Schryvers. Microstructure changes during non-conventional heat treatment of thin Ni–Ti wires by pulsed electric current studied by transmission electron microscopy. *Acta Mater* **58:** 4503-4515, 2010.

Microstructure and Failure Mechanisms of Reactor Pressure Vessel Austenitic Cladding

Jan Štefan[1,2], Jan Siegl[1], Radim Kopřiva[3]

[1]Department of Materials, Faculty of Nuclear Sciences and Physical Engineering,
Czech Technical University in Prague.
[2]Department of Impact and Waves in Solids, Institute of Thermomechanics of the CAS, v. v. i.
[3]Department of Mechanical Properties, ÚJV Řež, a. s.
jan.stefan@fjfi.cvut.cz

Abstract

Results of a thorough investigation of VVER-440 austenitic cladding will be presented herein. Specimens fractured in static fracture toughness tests were used for this purpose. Metallographic analysis provided information on the complex microstructure of the cladding. Fractographic analysis revealed mechanisms of crack propagation through the cladding. Conclusions on the relationship between the local microstructure, the failure mode and the fracture toughness of the cladding were drawn.

Keywords: Austenitic stainless steel; Metallographic analysis; Fractographic analysis; Fracture toughness.

Introduction

Nuclear reactor pressure vessel (RPV) of Russian water-cooled water-moderated VVER-type is composed of several structural materials, namely of a base metal (BM), a weld metal (WM) and an anti-corrosive cladding. As both the BM and the WM are ferritic steels with no particular corrosion resistance, austenitic cladding layer is deposited on the RPV inner surface, preventing direct contact of the BM and the WM with the coolant. In the case of VVER-440 reactor type, austenitic cladding is produced by submerged arc welding technology using strip electrodes. Total thickness of the cladding is about 8-10 mm and composes of layers of two austenitic stainless steels, namely of Sv 07Ch25N13 (the 1st cladding, deposited directly on the RPV wall) and of Sv 08Ch19N10G2B (the 2nd cladding, deposited subsequently). The cladding can significantly affect the RPV integrity, especially in the cases of accidents connected with over-cooling of the RPV. This fact stresses the importance of knowledge on mechanical properties of the cladding.

Experiments

Current experiments were based on the results of a number of static fracture toughness tests that were performed at the Department of Mechanical Properties of the ÚJV Řež, a. s. institute. Test specimens were of standard three-point-bend type with a fatigue precrack and were manufactured from the VVER-440 1st cladding (see Table 1 for contents of alloying elements). Fracture toughness values, being evaluated in the form of critical J-integral ($J_{0.2}$) in compliance with ASTM standard [1], exhibited a remarkable scatter. For instance, values ranging from c. 40 kJ m^{-2} to c. 400 kJ m^{-2} were determined in a narrow region of test temperatures of 24 and 50 °C. In order to assess causes of this behaviour, detailed investigation of the austenitic cladding microstructure and failure mechanisms was undertaken. Metallographic analysis of the material was performed. The microstructure was investigated using an optical microscope, a scanning electron microscope (SEM) in a backscattered electron detection mode, and an energy

dispersive X-ray spectroscopy (EDS) device. Besides, fractographic analysis was undertaken using a SEM in order to determine the mechanisms of crack propagation through the cladding.

Table 1: Contents of alloying elements in the austenitic steel of the first cladding layer of VVER-440 RPV [wt.%], as requested by [2]-standard.

material	C	Si	Mn	Cr	Ni	Mo	Ti	Nb	S	P	Cu
Sv 07Ch25N13 (1st cladding)	max. 0.09	0.3 1.2	0.8 2.0	22.0 26.5	11.0 14.0	–	–	–	max. 0.020	max. 0.030	–

Results and discussion

All the image documentation and the results presented herein are related to a specimen tested at 24 °C that reached a fracture toughness value $J_{0.2}$ of 149 kJ m^{-2}. Metallographic analysis revealed duplex austenitic-ferritic microstructure of the cladding. As can be seen in Figure 1, the microstructure showed a strong "solidification" character composed of cells and dendrites. Between the "classical cellular area" and the "classical dendritic area" (located in the vicinity of the weld fusion line, and at a greater distance, respectively), there was an unambiguously distinguishable transition region of several hundreds of microns in width.

The main crack propagation mechanisms were determined on the fracture surface. As the fracture toughness test started, the crack propagated through the cellular region by classical transgranular ductile "dimpled" fracture (see Figure 2A). As the crack front reached the transition region, an abrupt and change of fracture mechanism occurred (Figure 2B). Macroscopically, fracture surface could be estimated as ductile. However, features of some non-ductile secondary cracking were found at magnifications of 1000x and higher. Character of local fractographic features clearly implies low level of local plastic deformation, hence, low fracture energy consumption. This result bears evidence of crucial impact of the transition region (henceforth denoted as LTS – Low Tearing Strength – region) to the fracture toughness of the cladding and clarifies relatively low fracture toughness evaluated.

Further investigations were performed using a backscattered electron detection mode of a SEM. This revealed presence of large solidification-structure units being composed of a certain phase distinct from the δ-ferrite. Subsequent EDS analysis revealed a particular enrichment of this phase with chromium and silicon and a depletion with nickel. On the basis of this result and information in the literature [3], it could be identified as a σ-phase. This phase is characterized by a very complex tetragonal structure and an extreme hardness and brittleness. Clear evidence of identification of these objects as a sigma phase would require more thorough investigations, e.g. methods of crystallographic analyses. Nevertheless, the substantially elevated amount of this phase within the LTS region still remains the most demonstrable difference from both the cellular and the dendritic regions. This observation is plausible explanation for locally least tough fracture behaviour of the LTS region within the cladding.

Conclusions

The 1st cladding layer of a VVER-440 reactor pressure vessel was investigated. The material showed a duplex austenitic-ferritic microstructure with strong solidification character. Three regions could be discerned: a cellular region in the vicinity of the weld fusion line, followed by a transition region and a dendritic region. Crack propagation through the transition region was connected with much less ductile fashion of crack propagation than in the other regions. Elevated amount of brittle σ-phase in this transition region was found to be the most plausible reason for this behaviour. It could be concluded that the great variability of fracture toughness

values ($J_{0.2}$) detected in the series of fracture toughness tests could be attributable to fortuity of a precrack position with respect to this critical "Low Tearing Strength" transition region.
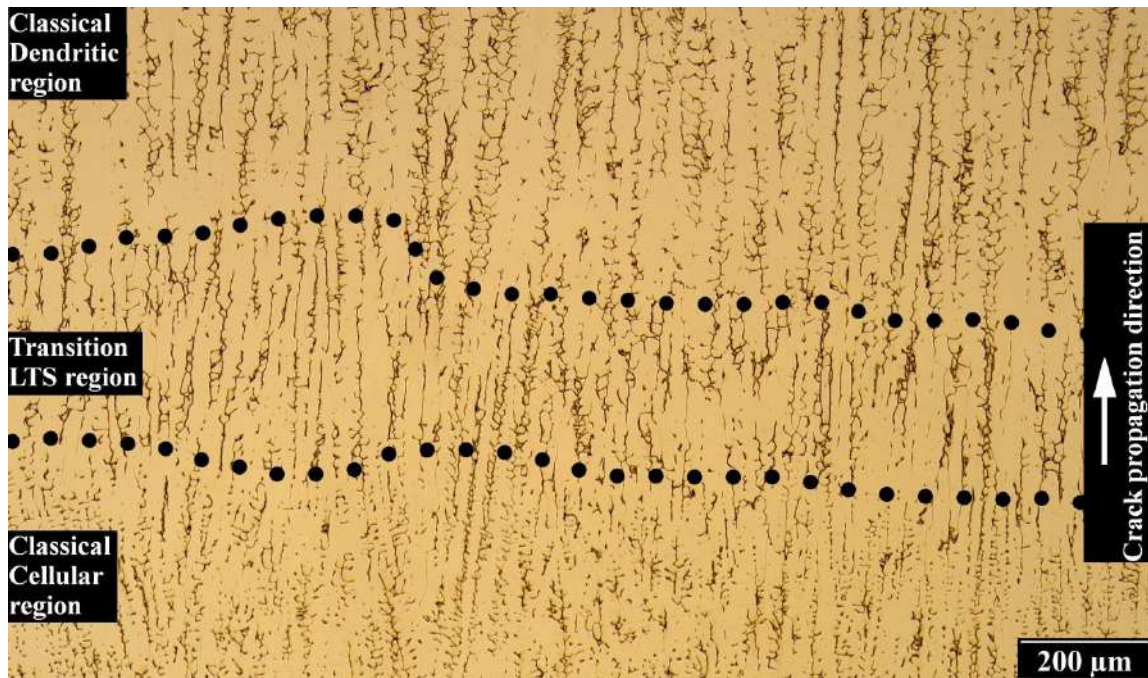

Figure 1: Microstructure of the 1st cladding in the area of crack propagation. The dotted lines separate the transition region of "Low Tearing Strength" from purely cellular and dendritic regions.
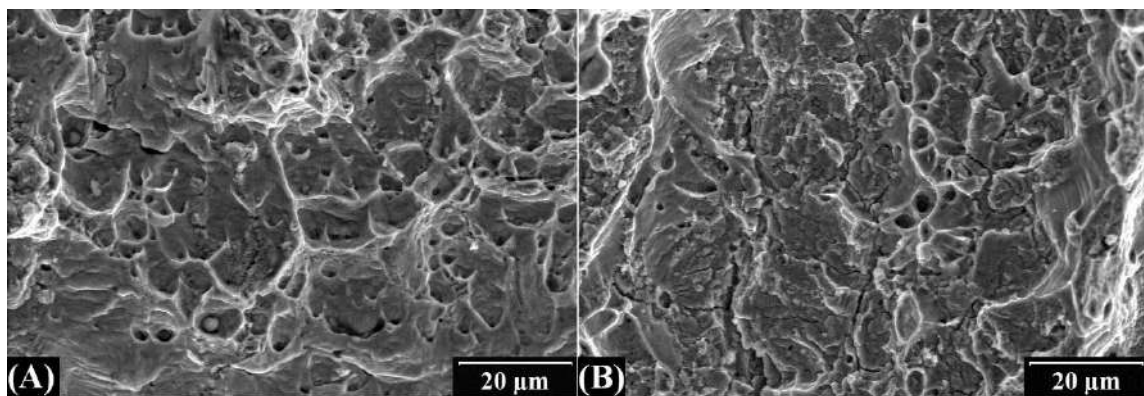

Figure 2: Characteristic features of transgranular ductile fracture of classical cell area (A) and features of fracture in the LTS-region (B).

References

[1] ASTM International. *Test Method for Measurement of Fracture Toughness. (ASTM E 1820-99a standard.)* West Conshohocken, USA, 1999, DOI: 10.1520/e1820-99a.
[2] Federal Inspection of Russia for Nuclear and Radiation Safety. *Equipment and Piping of Nuclear Power Installations. Weld Joints and Weld Overlays. Rules of Inspections. (PNAE G-7-010-89 standard.)* Moscow, 2000.
[3] J. M. Vitek, S. A. David. The sigma phase transformation in austenitic stainless steels. Welding Journal: 106-111, 1986.

Influence of Radiation Damage of Reactor Inner Components on the Results of Indentation Tests

Jan Ondráček, Aleš Materna

Department of Materials, Faculty of Nuclear Sciences and Physical Engineering, Czech Technical University in Prague
jan.ondracek@fjfi.cvut.cz

Abstract

Irradiation of inner components of the WWER reactor type made from austenitic steel 08Ch18N10T alters their material properties and may cause component degradation. Numerical simulations of the indentation test on the non- and neutron-irradiated reactor's inner components were carried out. The aim of this study is to find out whether the indentation test is suitable for assessing the material radiation damage of studied components.

Keywords: Neutron-irradiated material; Hardness; Indentation; WWER; FEM.

Introduction

The extent of radiation damage of reactor pressure vessel internals (RVI) is a key factor in determining of remaining life span of nuclear power plants. In the WWER reactors, parts of the RVIs are made from Ti stabilized austenitic stainless steel 08Ch18N10T. The overall radiation dose absorbed by the RVIs after 40 years of operation can exceed 40 dpa [1]. The neutron irradiation produces a series of defects in material. With contribution of other factors, such as a higher temperature, dislocation loops, precipitates, cavities and chemical changes on grain boundaries are formed over time.

This leads to changes in mechanical properties, namely an increase of yield stress and hardness and decrease of ductility. It is important to assess how the material properties change in dependence on the overall radiation dose. Since the irradiated material is scarce, hardness testing, which needs only little testing material compared to other testing methods, might be used to estimate material properties of irradiated materials.

Numerical simulations of hardness testing (HT) of non- and neutron-irradiated materials were made in this study in order to decide whether the HT can reliably estimate hardness of the studied material. The material used in this analysis is the 08Ch18N10T austenitic stainless steel withdrawn from the decommissioned WWER 440 NPP in Greifswald. Tensile tests of non- and neutron-irradiated samples with dose of 5.2 dpa conducted in 20°C air environment from [1, 2] were used as input for numerical finite element modelling of the indentation test.

Numerical modelling

A two dimensional axisymmetric FEM model was used to simulate the indentation test. A detail view of the finite element mesh is shown on Figure 1. The area of the sample where the indentation takes place is filled by four node quadrilateral elements with dimensions 5×2 μm, the rest of the specimen is filled by three node triangular elements. The indenter is modeled as a rigid body with no friction with the sample. Its equivalent cone apex semi-angle has been set to 70.3°. A cone indenter with this shape has the same projected contact area per penetration depth as the Vickers indenter.

The indentation process was driven by force with the maximum value 100 N.

The plastic response of the material was modeled using the isotropic hardening with von Mises yield condition. The yield stress of the non- and neutron-irradiated material was 230 MPa and 935 MPa respectively. The isotropic elastic properties were for both materials identical: Young moduli equals 200 000 MPa, Poisson ratios is 0.3. The work-hardening behavior of the non-irradiated material was described by the equation $\sigma = 1378(\varepsilon_{pl} + 0.0362)^{0.531}$. The true stress-true strain curves of the neutron-irradiated material showed no hardening effect therefore the elastic-perfectly plastic material model was used for the neutron-irradiated material. The above-mentioned material data were taken from [2].
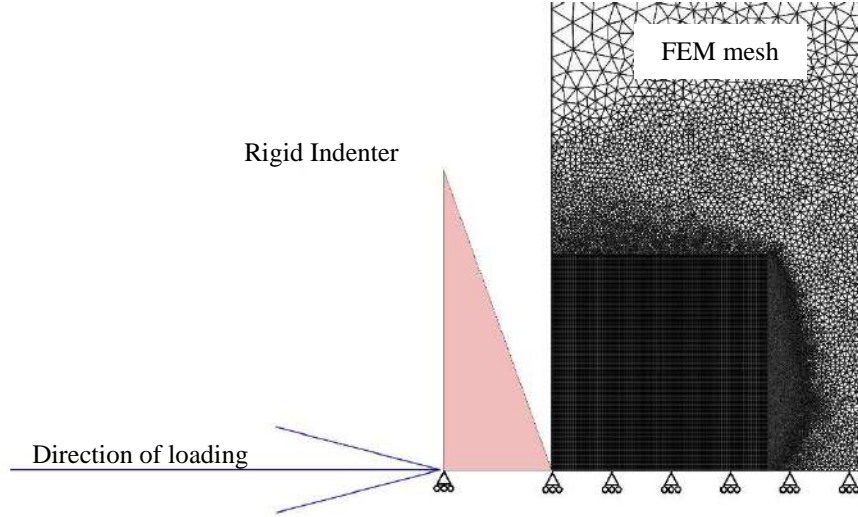
Figure 1: FEM model of the indentation test.

Results and discussion

The simulations of hardness testing were evaluated using a direct contact area method (CA) and the Oliver-Pharr method [3]. In case of the CA method, the radius of the circular projected contact area at maximal load was read directly from the results. The computed unloading force – penetration depth curves were used to obtain hardness by the OP method. The summary of the results is in the following table.

Table 1: Results of the hardness simulation for non- and neutron-irradiated material evaluated by the direct contact area method (CA) and the Oliver-Pharr (OP) method compared to the experimental hardness measurement.

	CA	OP	Experimental data [1]
Non-irradiated mat. [HV]	143	144	185±10
Irradiated mat., 5.2 dpa [HV]	276	322	363±9

The computed hardnesses are smaller comparing to the experimental data for both non- and neutron-irradiated material. The hardness of the irradiated material raised by a factor of 1.96 according to the experiment. The computed hardnesses of the irradiated material increased 1.93 times, resp. 2.24 times for the CA, resp. OP method. Higher values of hardness in case of the OP method can be explained due to the material pile-up at the surface caused by substantial plastic deformation under the indenter. The OP method uses only an elastic solution to evaluate the contact area and therefore overestimates the hardness when material pile-up occurs. An elastic-

perfectly plastic material model used in case of the irradiated material produces a higher pile-up than a material model with hardening. Therefore, the hardness ratio is higher in case of the OP method.

The increase of hardness, including the ratio factor, due to material irradiation is successfully predicted by the model. The absolute values of computed hardnesses are approximately 23% smaller comparing to the experiment. This can be due to slightly different mechanical properties of specimens for tensile and hardness testing. More indentation test simulations on irradiated materials need to be done in order to increase confidence in the presented model.

Conclusions

The following conclusions can be done from the presented work:
1. A simple 2D axisymmetric FEM model of the indentation test can be used for evaluating hardness changes in the 08Ch18N10T austenitic stainless steel due to neutron irradiation.
2. The indentation model gives 23% smaller values of hardness for both non- and neutron-irradiated material with dose of 5.2 dpa comparing to the experimental hardness tests.
3. The direct projected contact area method for calculating hardness is better suited for the irradiated steel than the Oliver-Pharr method for the reason that material pile-up at the indent causes inaccurate results.

References

[1] A. Hojná, et al. Irradiation assisted stress corrosion cracking of austenitic stainless steel WWER reactor core internals. In *15th International Conference on Environmental Degradation of Materials in Nuclear Power Systems-Water Reactors* (eds J. T. Busby, G. Ilevbare and P. L. Andresen). John Wiley & Sons, Inc., Hoboken, New Jersey, Canada.
[2] H.K. Namburi, et al. Effect of tensile strain on microstructure of irradiated core internal material. ENYGF 2015: European Nuclear Young Generation Forum 2015, France
[3] W. Oliver, G. Pharr. An improved technique for determining hardness and elastic modulus using load and displacement sensing indentation experiments. *J Mater Res* **7**(6): 1564–1583, 1992.

Deformation of Fe3Si Monocrystals Under Nanoindentation

Jaroslav Čech, Petr Haušild, Aleš Materna

Department of Materials, Faculty of Nuclear Sciences and Physical Engineering, Czech Technical University in Prague

Abstract

Mechanical properties and deformation mechanisms of differently oriented Fe3(wt.%)Si single crystals during spherical indentation are investigated. For correct interpretation of measured data and better understanding of the deformation mechanisms under loaded indenter tip, finite element simulations are carried out. Differences in indentation curves, mechanical properties and shapes of residual imprints are observed and associated with different activation of slip.

Keywords: Nanoindentation; Bcc; Crystallographic orientation; Slip systems.

Introduction

In last decades, nanoindentation became very important technique used for characterization of mechanical properties of various materials. Generally, it gives the values of the hardness and Young´s modulus. Nevertheless, studying whole indentation process and deformation mechanisms under the indenter tip could give additional information about investigated material.

Stress and strain fields, evolution of defects and dislocation movement under the indenter in the materials with crystallographic structure are very complex and difficult to evaluate or solve analytically. Thus, the computer models based on finite element (FE) method [1] or molecular dynamics [2] are usually employed.

In this study, indentation with spherical indenter was used to investigate body centered cubic (bcc) Fe3(wt.%)Si single crystal in two orientations. Finite element model was developed to explain the differences in measured mechanical properties and deformation mechanisms.

Experimental details

The single crystals of bcc Fe3(wt.%)Si, which serves as a model material of ferritic steels, were produced by the floating-zone melting technique. Properties of this material depends strongly on crystallographic orientation [3]. Samples for nanoindentation testing were oriented with the planes (100) and (110) parallel to the specimen surface – Figure 1. Surface was prepared by standard metallographic procedures and finished by electrolytic polishing to remove residual stresses in the surface layers.

Nanoindentation tests to maximum load 75 mN and 500 mN were carried out on Anton Paar NHT2 nanoindentation instrument with diamond spherical indenter with nominal radius 20 μm. Data were evaluated by Oliver-Pharr method [4] and residual imprints with activated slip systems were observed by optical and scanning electron microscope.

Elastic constants used in the elastic finite element model were taken from reference [5]. Hardness and Young´s modulus were determined for both material orientations and resolved shear stresses τ_{RSS} corresponding to all possible slip system for bcc structure (i.e. 48 slip systems for planes {110}, {112}, {123} and directions <111>) were computed using Schmid´s law.

Results and discussion

Example of experimental indentation *F-h* curves are shown in Figure 2. For the orientation (100), pop-in phenomenon (sudden increase of penetration depth) was observed. The value of force, for which the pop-in occurred, was very variable. For some curves, pop-in even did not occur, the curve was only elastic and no residual imprint was observed. It means that pop-in event is associated with the beginning of plasticity (nucleation of dislocations and activation of slip). On the other hand, elastic-plastic curves with nearly immediate activation of slip after the contact were also observed. If observed, the pop-ins were spread in the whole range of studied loads. For the orientation (110) only elastic-plastic curves were observed.

Hardness and Young´s modulus of this anisotropic material were measured experimentally and computed by finite element method. It was found by both methods that orientation (110) was slightly harder and stiffer than orientation (100).
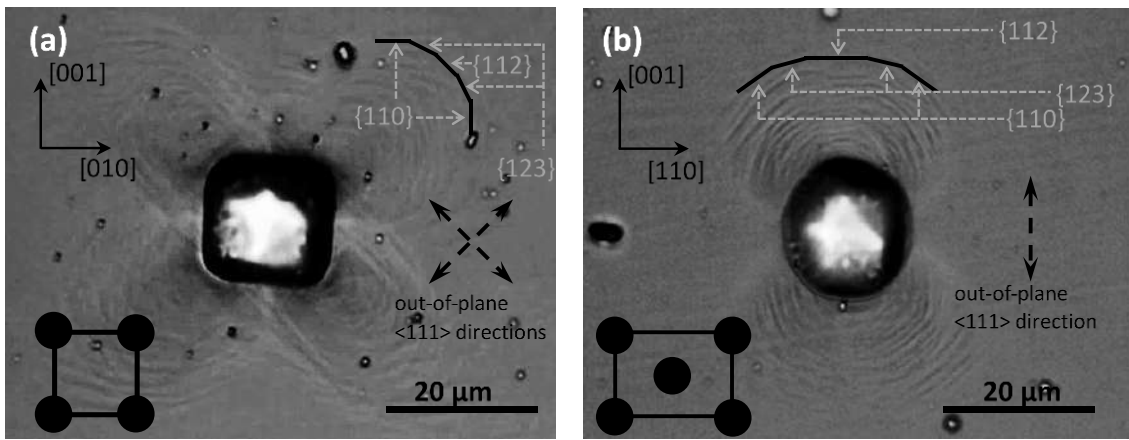
Figure 1: Residual imprint for (a) (100) and (b) (110) crystal orientation. Layout of atoms in surface layer is shown in left-down corner. Intersections of slip planes with the surface are shown.
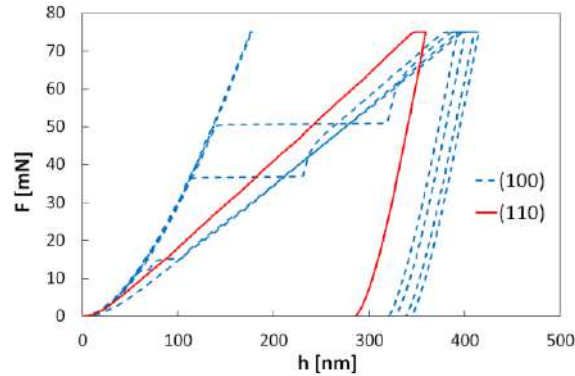

Figure 2: Experimental indentation curves for (100) and (110) orientations.

Images of residual imprints (indentations to 500 mN) are shown in Figure 1. For the orientation (100), four-fold symmetry is visible and shape of the imprint is more like a square than a circle. For the orientation (110) two-fold symmetry could be observed, shape of the residual imprint is more regular and the circle is only slightly elongated. The deformation spreads preferentially in <111> out-of-plane directions (<111> directions not lying in surface plane).

To explain the shape of the imprints and origin of slip lines visible on the surface, finite element simulations were performed. The difference in resolved shear stress for two studied orientations causes the difference in measured indentation curves. For the orientation (100),

resolved shear stress is approximately 1.5times lower than for the orientation (110). Thus, the slip systems are activated later, when higher loads are reached. Before it, the material is deformed elastically. Activation of slip systems can be then observed as a pop-in event. The dispersion of the load value, where pop-in occurs, could be caused by the preexistence of dislocations under the indenter. In the case of no pop-ins, τ_{RSS} is lower than the stress necessary for homogeneous nucleation of dislocations and thus, no plastic deformation is present. The intersections of the planes {110}, {112} and {123} with maximum resolved shear stresses and the surface are shown in Fig. 1a. They correspond well to the slip lines observed on the surface. The number of the active slip systems is enough high to enable the propagation of deformation in the preferred directions and as a result, the shape of the indent is more like a square than a circle.

For the orientation (110), the resolved shear stress is higher, thus the slip systems are activated at lower loads. As a consequence, the pop-ins are not observed in indentation curves and the material deforms plastically from the beginning of the test. The intersections of the planes {110}, {112}, {123} with maximum τ_{RSS} and the surface are shown in Fig. 1b and again, they correspond well to the slip lines observed on the surface. The number of the slip systems with maximum τ_{RSS} is only half of the systems for the orientation (100). It is not enough to enable the deformation only in <111> out-of-plane directions. Nevertheless, τ_{RSS} in other systems is high enough for their activation resulting in the deformation in other directions. Thus, the shape of the imprint is nearly spherical, only slightly elongated in the <111> out-of-plane directions.

Conclusions

In the present study, mechanical properties and deformation mechanisms of two Fe3Si (wt.%) single crystals were studied. It provided valuable information about the deformation behavior of anisotropic materials under nanoindentation, which is very complex and difficult for interpretation. It was found that hardness and Young´s modulus depend on the crystallographic orientation of the studied material. Finite element model confirmed that the orientation (110) is stiffer and harder than the orientation (100). The pop-in behavior, the shape of the residual imprints and the activation of slip systems were explained based on the evaluation of resolved shear stress computed by FE model.

References

[1] V. Gaspard, G. Kermouche, D. Delafosse, A. Barnoush. Hydrogen effect on dislocation nucleation in ferritic alloy Fe-15Cr as observed per nanoindentation. *Mater Sci Eng A* **604**: 86-91, 2014.

[2] R. Smith, D. Christopher, S.D. Kenny, A. Richter, B. Wolf. Defect generation and pileup of atoms during nanoindentation of Fe single crystal. *Phys Rev B* **67**: 245405, 2003.

[3] J. Prahl, A. Machová, M. Landa, P. Haušild, M. Karlík, A. Spielmannová, M. Clavel, P. Haghi-Ashtiani. Fracture of Fe-3 wt.% Si single crystals. *Mater Sci Eng A* **462**: 178-182, 2007.

[4] W.C. Oliver, G.M. Pharr. An improved technique for determining hardness and elastic modulus using load and displacement sensing indentation experiments. *J Mater Res* **7**(6): 1564-1583, 1992.

[5] A. Machová, S. Kadečková. Elastic constants of iron-silicon alloy single crystals. *Czech J Phys B* **27**: 555-563, 1977.

Problem of a Thorough Geometric Optimization

Tomáš Koubský

Department of Solid State Engineering, Faculty of Nuclear Sciences and Physical Engineering, Czech Technical University in Prague

Abstract

The usual problem when simulating chemical properties of molecules is finding the optimal structure of the molecular systems. In the case of CyMe$_4$BTBP, a highly promising organic extractant in partitioning of spent nuclear fuel, we optimized structures of the probable products of undesirable chemical reactions. The combination of molecular dynamics and quantum mechanics was used to find the most stable molecular structures. After determining the most probable reaction products, industrial improvements can be done to prevent the extractant's degradation.

Keywords: Density functional theory; Geometrical optimization; Gaussian; CyMe$_4$BTBPP.

Introduction

It has been shown that ligands with soft N-donor atoms can distinguish between the actinides and lanthanides – a crucial feature in the hydrometallurgical partitioning of spent nuclear waste. Among others, 6,6'-bis(1,2,4-triazin-3-yl)-2,2'-bipyridine ligands (BTBPs) with its representative CyMe$_4$BTBP (Figure 1) have emerged as particularly promising. In general, BTBP ligands can be considered as currently the most suitable ligands for the herein mentioned separation tasks. [1]

To evaluate the applicability of those ligands for process development, it is necessary to theoretically investigate their behaviour in the experimental conditions, particularly the mechanisms of degradation caused by contact with the highly reactive environment. In this paper, we present results of geometrical optimization of several degradation products – molecular structures emerging as a result of degradation reactions between the ligand and solvent (1-octanol).
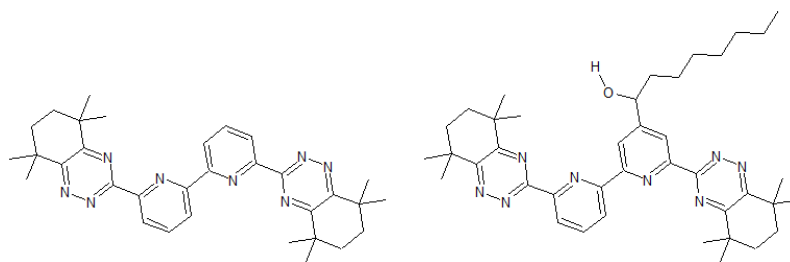

Figure 1: Organic extractant CyMe$_4$BTBP (left) and a schematic formula of the probable degradation product (right).

Computational Settings

For geometrical optimization, simulation methods based on Density Functional Theory (DFT) were used as implemented in the Gaussian 09 code, with the hybrid exchange-correlation

functional B3LYP and the 6-31G(d,p) basis set. The PCM cavity approximation of solvent is used with 1-octanol. [2]

To eliminate the risk of finding an incorrect local energetic minimum, pre-optimized by molecular dynamics (MD) was performed. For this purpose, the Amorphous Cell module [3] of the Material Studio 6.1 computational package was used to generate 6 cell configurations of the mixtures. The cells were equilibrated as canonical ensembles using the Forcite Plus module [4] over the time of 30 ps. The COMPASS forcefield and the combined ABNR and Quasi-Newton algorithms were used.

Results

Thanks to the HPLC-MS measurements of solutions with degraded CyMe$_4$BTBP [5], it is plausible to expect that during degradation, the adducts of CyMe$_4$BTBP and 1-octanol are being formed, depicted schematically in Figure 1 (right). However, the factual structure and conformation of the prevailing degradation product must be compared found after optimization and comparison of all possible alternatives.

The risk of finding an incorrect local energetic minimum is inevitable in all cases of geometrical optimization by quantum mechanical methods. This risk is even higher, when the small changes in molecular geometry have a significant influence on the calculated properties, such as total energy or orbital structure. One of the techniques to avoid this problem is pre-optimization by a simpler computational method, usually MD.

In such procedure, the chemical features based on electronic structure (such as orbital structure or chemical bonding) are not taken into account but the electrostatic interaction between the ligand and molecules of the solvent are simulated in a more realistic manner. When using MD, the computational methods are capable of incorporating hundreds of molecules and explicitly simulate more macroscopic behaviour of a ligand molecule surrounded by molecules of the solvent. Therefore, the ligands can more likely adopt a more realistic conformation. After that, there is higher probability that the consequent DFT optimization finds a lower and possibly global energetic minimum.

In this work, we used the Forcite code to simulate MD for a solution of CyMe$_4$BTBP and the expected degradation product in 1-octanol, as was performed experimentally [5]. After equilibration and MD of the system, we took a statistical sample of remaining molecular geometries of the CyMe$_4$BTBP degradation products as initial guesses for DFT optimizations. By this 2-step optimization procedure degradation products, we found conformations with approximately 0.5 – 3.5 kcal/mol lower energies than the ones optimized directly by DFT [6]. After such optimization, the degradation product presented in Figure 2 was determined as the most stable, with the energy approximately 3.3 kcal/mol lower than other options. One of the reasons for its lowest energy of formation is the creation of an intramolecular hydrogen bond, which was also found thanks to the thorough 2-step optimization.
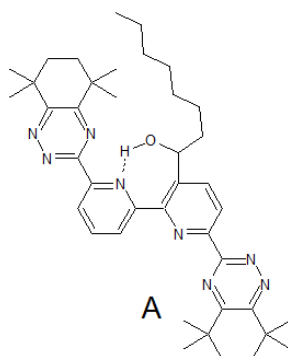
Figure 2: The most stable degradation product of CyMe₄BTBP in 1-octanol. The dashed line stands for an intramolecular hydrogen bond.

Conclusions

The problem of finding local energetic minimum during geometrical optimization is common for all quantum mechanical simulation methods. In this work, we optimized the probable degradation products of CyMe₄BTBP, a promising organic extractant used in partitioning of spent nuclear fuel. The 2-step MD-DFT optimization was performed and the most stable structure of the probable degradation product was found.

References

[1] A. Geist, C. Hill, G. Modolo, M. Foreman, M. Weigl, K. Gompper, M. J. Hudsond, 6,6'-Bis(5,5,8,8-tetramethyl-5,6,7,8-tetrahydro-benzo[1,2,4]triazin-3-yl) [2,2'] bipyridine, an Effective Extracting Agent for the Separation of Americium(III) and Curium(III) from the Lanthanides. *Solv Extr Ion Exch* **24**: 463-483, 2006.

[2] M. J. Frisch, et al. *Gaussian 09, Revision D.01*. Gaussian, Inc., Wallingford, 2009.

[3] P. J. Flory, *Statistical Mechanics of Chain Molecules*. Interscience, New York, 1969.

[4] O. Ermer, Calculation of molecular properties using forcefield applications in organic chemistry. In: *Bonding Forces*. Springer, Berlin Heidelberg, 1976.

[5] H. Schmidt, A. Wilden, G., Modolo, F., Bosbach, B., Santiago-Schübel, M. Hupert, H., Švehla, B., Grüner, C., Ekberg, Gamma Radiolysis of the Highly Selective Ligands CyMe₄BTBP and CyMe₄BTPhen: Qualitative and Quantitative Investigation of Radiolysis Products. *Proc Chem* **21**: 32-37, 2016.

[6] T. Koubský, H. Schmidt, G. Modolo, L. Kalvoda, Simulation of UV/Vis Spectra of CyMe₄BTBP and Some of its Degradation Products, *Proc Chem*, **21**:509-516, 2016.

Influence of As-Sb Substitution on $Cu_{12}Sb_4S_{13}$ Thermoelectric Properties

Petr Levinsky[1,2,3], Christophe Candolfi[3], Anne Dauscher[3], Bertrand Lenoir[3],
Jiri Hejtmanek[2]

[1]Department of Solid State Engineering, Faculty of Nuclear Sciences and Physical
Engineering, Czech Technical University in Prague
[2]Department of Magnetics and Semiconductors, Institute of Physics, Czech Academy of
Sciences
[3]Department of Physics and Chemistry of Surfaces, Institut Jean Lamour, CNRS,
Nancy, France
levinpet@fjfi.cvut.cz

Abstract

Current research on thermoelectric properties of the tetrahedrite family of materials, $Cu_{10}(Zn,Fe,Cu,\ldots)_2(Sb,As)_4S_{13}$, has focused on tetrahedrite, the Sb end-member, while data remain scarce for tennantite, the As end-member. In this contribution we investigate the influence of isovalent substitution of As on the Sb site. High temperature experimental data are presented for a $Cu_{12}Sb_{4-x}As_xS_{13}$ ($x = 0, 1, 2, 3, 4$) series of samples synthesized via the solid state route. We show that As has a small negative influence on the thermoelectric properties.

Keywords: Tetrahedrite; Tennantite; Thermoelectric material.

Introduction

Materials with poor ability to conduct heat are attracting attention due to their potential use as thermal barriers or in thermoelectric modules for either electrical generation or cooling. [1] In the latter area of research, several families of semiconductors have been identified over the last years, all of them demonstrating very low thermal conductivity values whose temperature dependence mimics that of amorphous alloys. Among them are tetrahedrites with a general chemical formula $Cu_{10}(Zn,Fe,Cu,\ldots)_2(Sb,As)_4S_{13}$. [2, 3] Combined with semiconducting-like properties, their extremely low thermal conductivity results in a favourably high dimensionless thermoelectric figure of merit ZT defined as $ZT = S^2/(\rho\kappa)T$ where T is the absolute temperature, S the Seebeck coefficient, ρ the electrical resistivity and κ the total thermal conductivity, which is the sum of a lattice contribution κ_l and an electronic contribution κ_e. We investigate the influence of isovalent substitution of arsenic for antimony on thermoelectric (TE) properties.

Experiment

A series of five samples was synthesized by solid state route: $Cu_{12}Sb_{4-x}As_xS_{13}$, $x = 0, 1, 2, 3, 4$. Stoichiometric amounts of pure elements (99.99 % for Cu, 99.999 % for Sb, As, S) were mixed under Ar atmosphere and sealed in evacuated quartz tubes. These were kept at 923 K for 12 hours. Resulting ingots were ground, cold pressed, annealed in sealed evacuated quartz tubes at 723 K for one week, and quenched.

Ground powders were sintered at 720–800 K using the SPS Dr. Sinter 515S apparatus. The obtained pellets were cut into pieces for further analyses: crystal structure and phase purity were checked by powder X-ray diffraction (XRD; Bruker D8 Advance, Cu K$_{\alpha 1}$), measurements of the Seebeck coefficient and electrical resistivity were performed simultaneously between 300 and 700 K with the four-point method using a ZEM-3 (Ulvac-Riko) apparatus. The thermal diffusivity α was determined with a laser flash Netzsch LFA 427 equipment. Thermal conductivity κ was calculated from the relation $\kappa = \alpha c_p \rho$, where c_p is the specific heat (calculated using the Dulong-Petit relation) and ρ is the density.

Results and Discussion

A Cu$_{12}$Sb$_{4-x}$As$_x$S$_{13}$, $x = 0, 1, 2, 3, 4$, series was successfully synthesized. XRD measurements confirm that the samples are composed mainly of the desired phase. A small amount of secondary phases is present: in Sb-rich samples ($x = 0, 1, 2$) a solid solution between famatinite and luzonite (tetragonal Cu$_3$(Sb,As)S$_4$) appears. In As-rich samples ($x = 3, 4$) enargite (orthorhombic Cu$_3$AsS$_4$) is seen. The cell parameter decreases by 0.041 Å with each additional As atom. This can be well explained by the smaller size of the arsenic atom. The value is close to 0.037 Å reported in [3].

High temperature thermoelectric properties of the samples are shown in Figures 1 and 2. Isovalent substitution of As for Sb was not expected to have a substantial effect on the transport properties. This is indeed the case, the figures show that the differences between the samples are small. Caution therefore has to be taken when interpreting the data because of measurement uncertainty.

The Seebeck coefficient shows metallic behaviour for all the samples and rises linearly with increasing temperature. With each additional As atom S drops by some 3 %, deteriorating TE properties. Resistivity shows metallic behaviour as well but the absolute values are too close to confidently tell a trend, around 10^{-5} Ω.m at 300 K. We can tentatively say that ρ seems to drop between the $x = 0$ and $x = 1$ samples and then slowly rise with increasing As content before reaching a similar value for $x = 4$ as for $x = 0$.

Total thermal conductivity is around 1.3 W.m^{-1}.K^{-1} for all the samples in the whole temperature range. The electronic part κ_e is dominant, especially at high temperatures.
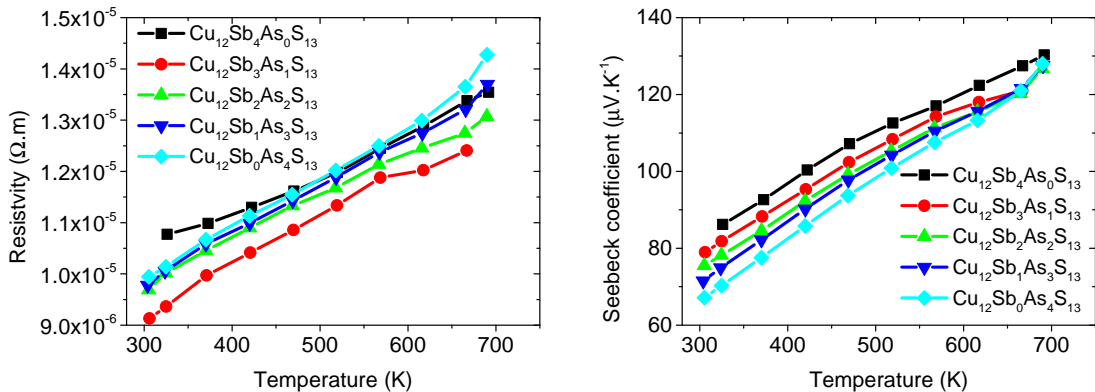

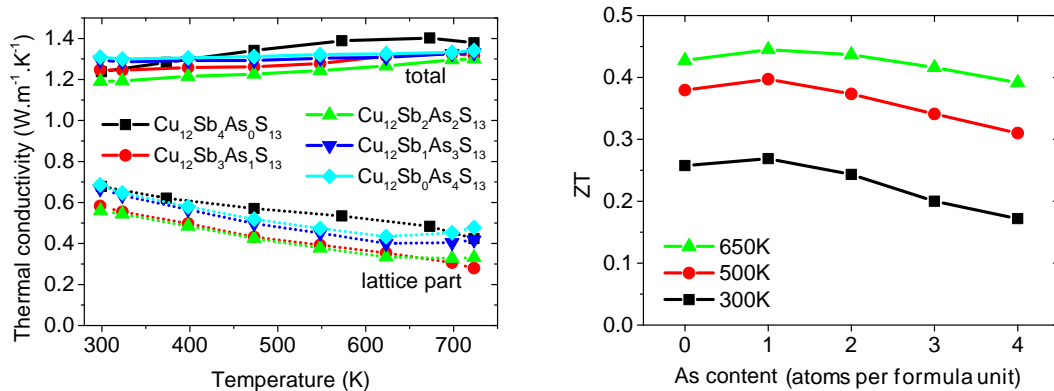Figure 1: Temperature dependence of the electrical resistivity and Seebeck coefficient.

Figure 2: Left: temeprature dependence of the thermal conductivity. Right: dependence of the figure-of-merit ZT on arsenic content.

Figure 2 shows that κ_l seems to reach slightly lower values for $x = 1, 2$. This observation would be consistent with increased phonon scattering due to mass fluctuation on the Sb/As site. We cannot, however, be completely sure that its origin is not an experimental error.

The values of ZT are again very similar, reaching a peak value around 0.6 at 720 K for all samples. ZT drops slightly with increasing As content mainly because of the decreasing Seebeck coefficient: for the pure As sample the peak value is 10 % lower than for the pure Sb one. Samples with $x = 0 - 2$ perform the best because of the slightly lower values of ρ and κ for $x = 1, 2$.

Conclusions

We successfully synthesized a series of tetrahedrite samples with different levels of As substitution. Only a small amount of secondary phases was detected. Isovalent substitution of arsenic for antimony only has a small effect on electrical and thermal properties of tetrahedrite. Its overall influence on the thermoelectric properties is slightly negative.

References

[1] X. Lu, et al. Tetrahedrites: Earth-Abundant Thermoelectric Materials with Intrinsically Low Thermal Conductivity. In *Materials Aspect of Thermoelectricity*, chap. 16. CRC Press, Boca Raton, 2016. doi:10.1201/9781315197029-17

[2] K. Suekuni, et al. Thermoelectric Properties of Mineral Tetrahedrites $Cu_{10}Tr_2Sb_4S_{13}$ with Low Thermal Conductivity. *Appl Phys Express* **5**: 051201, 2012. doi:10.1143/APEX.5.051201

[3] N. E. Johnson, et al. Compositional trends in tetrahedrite. *Can Mineral* **24**: 385-397, 1986.

Molecular Dynamics Simulations of Poly(dimethylsiloxane) Elasticity

Jaroslava Fojtíková

Department of Solid State Engineering, Faculty of Nuclear Sciences and Physical
Engineering, Czech Technical University in Prague
jaroslava.fojtikova@fjfi.cvut.cz

Abstract

This paper deals with mechanical properties of poly(dimethylsiloxane) (PDMS).
The material is easy to fabricate, thus it is often used in scientific laboratories and
industry. Our laboratory is focused on preparation of planar waveguide with a PDMS
cladding. There is observed an interesting mechanical behaviour of produced samples.
The main goal of the research is to describe relationship between PDMS crosslink-
ing level and elasticity using molecular dynamics simulations. The calculations were
performed within Materials Studio environment.

Keywords: Molecular dynamics; Diffusion coefficient; Elastic constants.

Introduction

The laboratory of applied photonics at FNSPE is focused on optic sensors. The chemical
fibre sensor with a different internal structure are tested here and the laboratory is also
equipped with a facility for preparing planar optic sensors. These sensors can measure a
low concentration of gases (in the first place, NH_3) and their second cladding is built from
PDMS.

In the last few years, the PDMS is extensively used in microfluidics and imprinting
techniques. The polymer is deformable (very small forces could be measured) and it easily
keeps the shape of a form pattern with a great differentiation (in the nm). Due to these
mechanical properties, there is growing presence of the PDMS in lab-on-a-chip or MEMS
devices (microelectro- mechanical system) [1]. Furthermore, it is inexpensive and very
easily to fabricate at a wide range of crosslinking percentage. Thus it is very popular in
both science and industry.

As mentioned above, the planar sensors with the PDMS cladding were tested and a
high sensitivity to small changes in ambient pressure was observed. We assume that this
effect could be caused by change of polymer elasticity at different crosslinking rate or due
to H_2O vapours adsorbed on PDMS surface.

This research is focused on verifying the first hypothesis using molecular dynamics
simulations. The elasticity of a polymer is a very complex problem, so for simplicity we
ignore a surface effects and try to map bulk modulus dependency on crosslinking rate only.

Computational Settings

The basis of molecular dynamics simulations are the classical equations of motion. They
are modified to deal with the effects of temperature and pressure on a system (defined
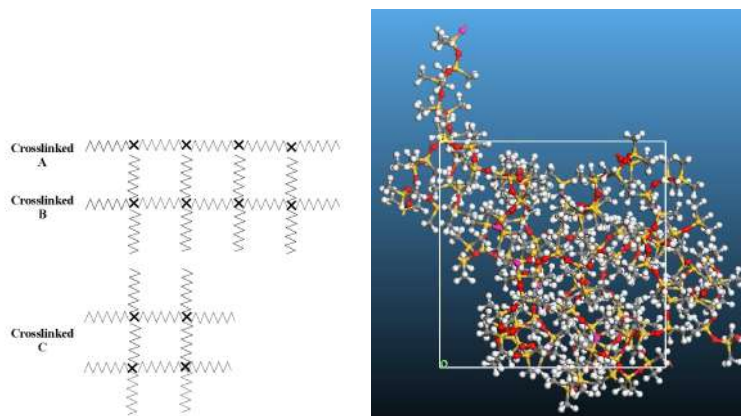statistical ensemble, NPT).

Figure 1: Left - the schema of PDMS models with different topology. Right - a cubic structure of the model using periodic boundary conditions.

Our system consists of one large molecule of PDMS with different topology as shown in Figure 1 - left. This molecule (as a group of linear and crosslinker fragments) is put into a cubic cell of defined density (0.965 g·cm^{-3}, [2]) using module MS Amorphous Cell. The crosslinker fragment is chosen in accordance with composition of commercial Sylgard 184 resin (Dow Corning).

After that the fragments are jointed together using special program simulating a condensation reaction of polymer controlling physical properties as volume and temperature. Inter- and intramolecular forces in the system are described by Compass II force field that is the most validated and used for polymers and composite materials. Surface effects are eliminated due to the implemented periodic boundary conditions of the cell.

Then, the cubic structure (Figure 1 - right) is geometrically optimized (ABNR and Quasi-Newton methods) and annealed in the temperature range 200-600 K in order to confirm presence of a global energetic minimum of the system. After that, molecular dynamics of canonical ensemble (N,V,T = constant) is performed on the prepared testing samples at room temperature.

Finally, NPT dynamics is used to compress the testing samples to the defined pressure and temperature states (0.1, 0.4, 0.8, 1.0 GPa, 298 K), under control of the Berendsen barostat and Nose thermostat methods.

The bulk moduli of the equilibrated structures are analyzed using the constant strain method with the strain of 0.3% applied in six basic directions of cubic cell. The whole procedure did not provide an equilibrated structure at the desired pressure level of 0.1 MPa, thus the K modulus was estimated according to the formula $K = \rho_0(dP/d\rho)_{\rho_0}$ where ρ_0 is the experimental density at the given T and the fixed number of monomer units present in the chain fragments.

Results and Discussion

The newest experimental values of elastic modulus of PDMS reported for the Sylgard 184 resin prepared under standard recommended conditions (curing time and temperature) vary from 0.1 to 1.75 MPa with the crosslinking ratio growing from 1.96 to 9.0 wt%. These results were obtained from macroscale compression tests and microscale nano-JKR

Table 1: Dependence of the elastic parameter K on the crosslinking ratio with detailed parameters of NPT MD.

	Cross A	Cross B	Cross C
Crosslinking [wt %]	25	13	11
K [MPa]	(0.81±0.15)	(0.75±0.10)	(0.55±0.16)

experiments. [3]

If we assume an isotropic structure and the Possion's ratio of PDMS ca. 0.45 [3], the bulk modulus should amount ca. 6 MPa. The latter value is expected to be rising up with the crosslinking ratio growing. The simulated values of the K modulus calculated for three selected topologies are summarized in Table 1.

In spite of performing the K modulus calculations on the most equilibrate structures, the obtained values are still underestimated and the system seems to be 'softer' than real experimental samples. On the other hand, the calculations confirmed the expected increase of K with the rising crosslinking ratio value.

Conclusions

The results seem to indicate that elastic properties of PDMS depend in the major extend on the crosslinking ratio and the particular network topology is of a less importance. This hypothesis will be verified on more extensive models featuring a range of different and more complicated topologies.

In the future, we plan to simulate elasticproperties of PDMS using mesoscale or finite element analysis methods compatible with the known viscoelastic behavior of PDMS, the viscoelasticity might be one of the reasons why K modulus values are systematically underestimate in the MD simulations.

References

[1] F. Schneider, T. Fellner, J. Wilde, U. Wallrabe. Mechanical properties of silicones for MEMS. *J Micromech Microeng* **18**, 2008.

[2] J. C. Lottersy, W. Olthuis, P. H. Veltink, P. Bergveld. The mechanical properties of the rubber elastic polymer polydimethylsiloxane for sensor applications. *J Micromech Microeng* **7**: 145, 1997.

[3] A. Sharfeddin, A. A. Volinsky, G. Mohan, N. D. Gallant. Comparison of the macroscale and microscale tests for measuring elastic properties of polydimethylsiloxane. *J Appl Polym Sci* **32**: 42680, 2015.

Alternative Methods of Permeation Barrier Preparation

Jakub Veverka[1,2], Jiří Matějíček[1]

[1]Department of Materials Engineering, Institute of Plasma Physics, Czech Academy of Sciences
[2]Department of Materials, Faculty of Nuclear Sciences and Physical Engineering, Czech Technical University in Prague
veverka@ipp.cas.cz

Abstract

Permeation barriers represent one of the crucial fields in materials development for thermonuclear fusion. Primary objective of the barriers is to suppress the permeation of hydrogen isotopes (mainly tritium) from future thermonuclear fusion facilities. Secondary objective is to reduce their retention in structural materials. Expected reactor conditions put high demands on the material, as well as on the final barrier quality. Key properties are tritium permeation reduction, absence of defects (especially cracks), high-temperature stability and corrossion resistance, and compatibility with structural materials (mostly ferritic-martensitic steels). Thin nitride layers, identified as promising permeation barriers, were prepared by diffusion-based nitridation and physical vapour deposition (PVD), and characterized.

Keywords: Permeation barriers; Nitride layers; PVD coating; Permeation measurement.

Introduction

Nuclear fusion is an appealing means of energy production that can resolve growing energy demands of the mankind with respect to the exhaustion of fossil fuels. Enormous complexity and demands (technological, as well as economical) on the fusion facilities delayed the harnessing of thermonuclear fusion, but joint international effort resulted in the construction of International Thermonuclear Experimental Reactor (ITER) that should demonstrate the feasibility of fusion and test all the facilities for future fusion powerplants. Permeation barriers are one of the most important parts of fusion facility concerning radiological safety and economical issues. These are typically thin coatings (commonly oxidic ceramics [1, 2] or nitrides [3, 4]) that lower the permeation and retention of hydrogen isotopes (mainly tritium) in the reactor structures. Excessive tritium permeation could result in

- Degradation of the reactor material properties.
- Radiological hazard during operation and decommisioning.
- Lowering of the reaction probability and economical losses.

Therefore the presence of a permeation barrier is envisaged by numerous studies [1, 5, 6] to meet the safety requirements of maximal allowable tritium losses (1g per year) and maximal tritium inventory (200g) [7]. In this study, diffusion-nitrided layers and PVD coatings were prepared and characterized. In addition, hydrogen permeation through the PVD coatings was measured.

Experiment

Diffusion-based nitride layers were prepared at Technical University of Liberec and by two industrial companies: Bodycote HT, s.r.o and Katring Plus s.r.o. As a substrate, ferritic-martensitic steel P92 (9%Cr-1.74%W-0.5%Mo) was used. Nitride layers were prepared by several means: plasma nitridation (430°C, 24h), carbonitridation (560°C, 10h) and salt nitridation (530°C). Presence of the nitride layer and its composition was investigated by Energy Dispersive Spectroscopy (EDS) and X-ray diffraction (XRD). Samples were annealed for 1 hour at 550°C to assess thermal stability of the coatings.

PVD coatings were prepared by magnetron sputtering at Department of Materials Engineering (Faculty of Mechanical Engineering CTU Prague) and by cathodic arc plasma deposition at IonBond Czechia s.r.o. As a substrate, Reduced Activation Ferritic Martensitic steel EUROFER (9%Cr-1.2%W-0.2%V-0.14%C), developed as a reference structural material for DEMO, was used. In total, 6 nitrides were deposited - CrN, Cr_2N, CrAlN, CrWN, WN, ZrN. Composition of the coatings was confirmed by EDS, thickness was measured by calotest method. Furthermore, phase composition was determined by XRD and adhesion of the coatings was measured by scratch test. Permeation measurements were performed at the facility of Jožef Stefan Institute in Ljubljana, Slovenia; at 400°C and 1bar H_2.

Results

EDS and XRD measurements of the diffusion nitrided coatings confirmed presence of the nitride layer. Thickness of the coatings, provided by the manufacturer, reached approximately 100 µm. However, XRD measurements after the annealing showed that the nitride layer was significantly decomposed. Therefore, permeation measurements of these layers were not performed.

Successful deposition of the PVD coatings was confirmed by EDS and XRD measurements. Thickness of the coatings was within the desired margin: 1.5 to 4.5µm. Scratch test showed good adhesion of all coatings with the exception of CrAlN. Repeated testing after the permeation measurements yielded slightly lower value for all coatings. XRD measurements indicated all the PVD coatings to contain compressive stress, which is favorable as it suppresses crack propagation. All the PVD coatings showed potential for permeation barriers with PRF (permeation reduction factor) > 100, in case of ZrN even > 10000. Phase stability after the permeation test was verified again by XRD.

Conclusions

Thin nitride layers were prepared by plasma nitridation, carbonitridation and salt nitridation. XRD measurements confirmed nitride layer formation (approximate thickness 100 µm, provided by manufacturer), however the layers were significantly decomposed after annealing. Therefore, hydrogen permeation was not measured. PVD coatings of selected nitrides were deposited on reference material for DEMO construction. The composition, thickness and adhesion of the coatings was measured and permeation measurements were performed. Thickness of the coatings was several µm, all coatings showed desired composition and good adhesion. Permeation measurements confirmed suitability

of selected nitrides as permeation barriers. Best result was achieved by ZrN, permeation reduction by 4 orders of magnitude.

References

[1] R. A. Causey, et al. Tritium barriers and tritium diffusion in fusion reactors. In *Comprehensive Nuclear Materials*, chap. 4.16. Elsevier, 2012.

[2] H. Glassbrenner, et al. Hydrogen permeation behaviour of hot-dip aluminized MANET steel. *Fusion Technol* **28**: 1159-1164, 1995.

[3] K. S. Forcey, et al. The formation of tritium permeation barriers by CVD. *J Nucl Mater* **200**: 417-420, 1993.

[4] I. L. Tazhibaeva, et al. Hydrogen permeation through steels and alloys with different protective coatings. *Fus Eng Des* **51-52**: 199-205, 2000.

[5] M. Abdou, et al. Blanket/first wall challenges and required RD on the pathway to DEMO. *Fus Eng Des* **100**: 2-43, 2015.

[6] D. Demange, et al. Tritium management and anti-permeation strategies for three different breeding blanket options foreseen for the European PowerPlant Physics and Technology Demonstration reactor study. *Fus Eng Des* **89**: 1219-1222, 2014.

[7] L. M. Giancarli, et al. Overview of the ITER TBM Program. *Fus Eng Des* **87**: 395-402, 2012.

Coatings Prepared from Liquid Feedstock Using WSP-H Plasma Torch

Tomáš Tesař[1,2], Radek Mušálek[2], Jan Medřický[1,2], František Lukáč[2], Jiří Kotlan[2]

[1]Katedra materiálů, Fakulta jaderná a fyzikálně inženýrská, České vysoké učení technické v Praze
[2]Oddělení materiálového inženýrství, Ústav fyziky plazmatu AV ČR, v. v. i.
tesarto1@fjfi.cvut.cz

Abstract

Plasma spraying with liquid feedstocks is quickly becoming a promising alternative to the conventional plasma spraying of coarse powders owing to the fact of being able to refine the microstructure of plasma-sprayed coatings up to the submicron range. This offers improved coating properties in terms of e.g. mechanical resistance, thermal protection, etc. The aim of this paper is to present some of the recent results of plasma spraying from liquid feedstocks with WSP-H plasma torch.

Keywords: Suspension plasma spraying; WSP-H; Microstructure; Mechanical properties.

Introduction

Liquid feedstocks (i.e. suspensions and solutions) are becoming a promising equivalent to dry coarse powders for the thermal spray technique [1]. In terms of functional performance, the coatings from liquid feedstocks show e.g. higher hardness, wear resistance, and tensile adhesion strength or lower thermal conductivity than the conventional counterparts [2].

However, the deposition from liquid feedstocks involves many parameters to consider in order to prepare an optimized coating. One of them is the carrier liquid (solvent), which influences the formation of the coating [3]. Water and ethanol are commonly used. The former is convenient for its availability (i.e. low price) and easy handling requiring no safety precautions, whereas the latter offers lower specific and latent heats, and even positive contribution to the thermal balance of the plasma-liquid interaction due to its possible combustion in the presence of ambient atmosphere [4]. Another parameter is the particle size of the powder to be dispersed in the solvent. Fine nanometric powders (mean particle size about tens of nanometers) can be used in order to reach the fine structure of the coating. However, due to their high specific surface, fine powders make it difficult to prepare a suspension with concentration higher than approximately 20 wt.% because of the high viscosity of the suspension [5]. On the other hand, coarser powders (mean particle size about units of micrometers) which allow concentrations of more than 50 wt.% are more difficult to stabilize in terms of the suspension sedimentation, since it is more difficult to overcome the gravitation force (e.g. by Brownian motion) and the particles tend to settle down to the bottom of the containing tank [5]. Therefore, chemical components like plasticizers or stabilizers are often added to the suspensions in order to improve their fluidity or stability, respectively.

Upon selection of the suspension formulation, it is necessary to find the optimal parameters of the spraying setup.

This paper aims to demonstrate the evolution of the spraying setup of alumina-based suspensions with WSP-H plasma torch using two suspension formulations and four deposition setups.

Materials and Methods

For the deposition experiments, two ethanol-based custom-made suspensions were used. For the primary experiments, 50 nm powder (Allied High Tech Products, INC, USA) was used to prepare the suspension with 20 wt.% concentration of the powder. For the optimized deposition, 300 nm powder (Allied High Tech Products, INC, USA) was used with 10 wt.% concentration along with a stabilizing agent BYK-LP C 22587 (BYK-GARDNER GmbH, Germany) in 0.5 wt.% concentration. Both suspensions were prepared by adding the required amount of powder to the solvent until the preselected concentration was reached. Afterwards, the suspensions were subjected to one hour milling with a set of crushing balls in order to break agglomerates of the powder particles.

Deposition was carried out using the hybrid gas/water stabilized WSP-H 500 plasma torch (ProjectSoft HK, a.s., Czech republic) according to parameters listed in Table 1. The torch was mounted on a programmable robot arm and operated at 150 kW power (500 A).

Vickers hardness was measured using Nexus 4504 (Innovatest, Netherlands) hardness tester using 0.3 kg load. For the hardness value evaluation, the indents diagonals were measured from SEM micrographs.

Table 1: Deposition parameters.

Deposition parameters	Spraying distance [mm]	Feeding distance [mm]	Nozzle diameter [mm]	Suspension concentration [wt.%]	Powder size [nm]
Experiment 1	100	25	0.5	20	50
Experiment 2	100	19	0.5	20	50
Experiment 3	100	19	0.35	20	50
Experiment 4	100	25	0.35	10	300

Results and Discussion

Cross-sections of the prepared coatings are shown in Fig. 1. In sections a) through c), the coating consisted mainly of spherical particles interconnected by soft feathery structures appearing darker in the SEM micrograph. These features originated probably from overheating and evaporation of part of the solid material injected into the plasma jet which were then redeposited onto the substrates. The spherical particles visible in the coatings in Fig 1a though 1c were thoroughly melted and re-solidified before impact onto the substrate. In terms of deposition parameters of Experiment 1 through Experiment 3 it was observed that decrease in the feeding distance (Experiment 1→Experiment 2) led to more intensive heating of the feedstock resulting in more powdery deposit embedded in the coating. The further decrease in the amount of the injected material (i.e. decrease in the injection nozzle diameter, Experiment 2→Experiment 3) only promoted the evaporation of the powder since more heat was available to the lower amount of suspension.

Fig. 1d (Experiment 4) clearly shows that the change of the feedstock suspension dramatically changed the nature of the coating. Instead of individual spherical particles, well-flattened splats are observable in the cross-section. The splats are mostly well-connected and the splat boundaries are difficult to identify.
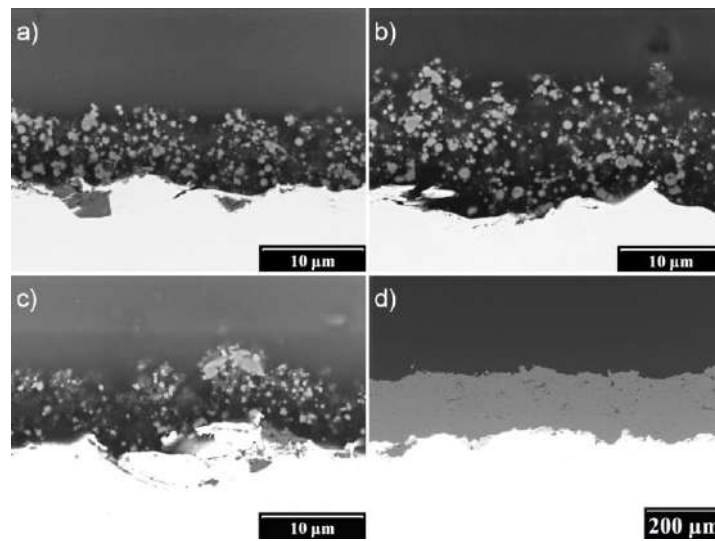
Figure 1: SEM micrographs (backscattered electrons detection) of cross-sections of the prepared coatings, a) Experiment 1, b) Experiment 2, c) Experiment 3, d) Experiment 4.

Due to low internal cohesion of the coatings from Experiments 1,2,3, hardness was measured for the Experiment 4 coating only. The value of 1211 ± 11 HV0.3 documents the exceptional bonding of the splats. Compared to the typical hardness value of a powder-sprayed alumina coating of approximately 900 HV0.3, the value of the novel coating is about 30% higher which means a significant improvement in the performance of the coating.

Conclusions

Comparison between coatings prepared from two different suspensions under several deposition conditions showed that submicron powder suspensions are more suitable for deposition using WSP-H plasma torch than nanometric powder ones. The coating prepared from the coarser 300 nm powder suspension showed remarkable value of Vickers hardness (1211 ± 11 HV0.3) compared to the soft character of the finer 50 nm powder suspension coatings.

References

[1] P.L. Fauchais, J.V.R. Heberlein, M.I. Boulos. *Thermal Spray Fundamentals*, 2014.
[2] T. Tesar, et al., Development of suspension plasma sprayed alumina coatings with high enthalpy plasma torch, *Surf Coat Technol* **325**: 277–288, 2017.
[3] P. Fauchais, et al. Operating parameters for suspension and solution plasma-spray coatings, *Surf Coat Technol* **202**: 4309–4317, 2008.
[4] M. Hlina, et al. Diagnostics of Hybrid Water/Argon Thermal Plasma Jet with Water, Ethanol and Their Mixture Injection to Plasma, *Plasma Phys Technol* **3**: 62–65, 2016.
[5] T. Tesař. Plazmové stříkání Al2O3 suspenze, Práce na výzkumném úkolu ČVUT Praha 2015.

Evolution of Monoclinic Twins After Type II Single Twin Boundary Passage in Ni-Mn-Ga Alloy

Vít Kopecký[1,2]

[1]Department of Solid State Engineering, Faculty of Nuclear Sciences and Physical Engineering, Czech Technical University in Prague
[2]Department of Magnetic Measurements and Materials, Institute of Physics, Czech Academy of Sciences
kopecvi1@fjfi.cvut.cz

Abstract

The high mobility of a/c twin boundaries in martensite of Ni-Mn-Ga alloy is unique phenomenon which can be used in various applications, e.g. actuation. In this experimental work we used optical microscope to study interaction between monoclinic twins and single type II twin boundary in order to evaluate affect of monoclinic twins on mobility of type II boundary. We showed that monoclinic boundaries are macroscopic and propagate through the bulk sample. We also showed that few passages of type II boundary did not change the monoclinic boundary.

Keywords: Monoclinic twinning; Ni-Mn-Ga alloy; Magnetic shape memory effect.

Introduction

Magnetic shape memory effect was first described in more than twenty years ago [1]. It was revealed that the effect is caused by highly mobile twin boundaries (interfaces). From that time, a lot of effort was put into describing the complexity of the twin boundaries, their interaction and mobility [2, 3].

In 10M martensite of Ni-Mn-Ga alloy three twinning levels differing in their scale can be found [3]. Macroscopic a/c twin boundaries are highly mobile and their mobility produces reorientation of microstructure. Due to the reorientation, the material produces a reversible deformation of several percent. This is the most promising effect of magnetic shape memory phenomenons. Moreover, a/c twin boundary can occupy two classes of planes: {101} and approximately {10 1 10}. The boundary occupying the former class is called type I twin boundary and the latter type II twin boundary. They also differ by their mobility, i.e. external stress (also called twinning stress) needed to be applied to achieve deformation by twin boundary motion. Twinning stress of type II is about 0.1 MPa which is approximately ten times more mobile than type I twin boundary. Both types are observable by optical microscope [4].

Twin boundaries occupying mesoscopic scale are called monoclinic (or modulation) twin boundaries [3]. They are also observable using optical microscope. Finally, a/b twinning can be found at microscale as it was recently for the first time observed using scanning electron microscopy (SEM) [5]. This type of twinning is under accessible resolution of optical microscopy.

All levels of twinning can exist at the same time in the material and they form more or less coherent interfaces that intersects each other and interacts together. One can imagine

how much complex the system is and how difficult it is to describe interactions in all levels to understand mechanism of a/c twin boundary motion.

In this work we used optical microscope to study an interaction between the macroscopic and mesoscopic types of twins. For that we chose the most simple case which is a single type II twin boundary passing through few monoclinic twin boundaries.

Experiment

The experiment was done on single crystal of $Ni_{50}Mn_{28}Ga_{22}$ (at. %) which was produced by modified Bridgman method in Adaptamat Ltd. The crystal of this stoichiometry is at room temperature in stable 10M martensitic phase which is monoclinic with the following lattice parameters a = 0.5843 nm, b = 0.5974 nm, c = 0.5589 nm, $\alpha = \beta = 90$, $\gamma = 90.34$ degrees.

We used optical microscope Zeiss in order to study macroscopically monoclinic twins and their interaction with single mobile a/c twin boundary. Circular Differential Interference Contrast (C-DIC), also known as Nomarski contrast, was used to visualise surface tilt by false colours. The monoclinic twin boundaries produce the surface tilt only in variant with c-axis in plane. In variant with c-axis oriented out of plane the monoclinic boundary produce no surface tilt, therefore we used a polarization contrast. The polarization contrast is yielded due to different optical activity of variants.

In our experiment, first, we took micrographs of monoclinic twins in compressed state, i.e. in variant with c-axis in plain. In contrast to previous papers, we took micrographs also from the opposite side of the sample to study macroscopic nature of monoclinic twins. After that we formed type II twin boundary and moved it across the sample by small tensile stress, i.e. the microstructure was reoriented due to the a/c twin boundary passage. Only type II twin boundary is compatible with this orientation of monoclinic twins [2]. The monoclinic twins in variant with c-axis out of plane do not produce surface tilt, however, polarized light can be used to visualise them. To enhance the weak contrast in the image of polarized contrast, we applied threshold filter. All micrographs are presented in Figure 1 as *before* twin boundary passage, *after* twin boundary passage and, finally, *after + TF* twin boundary passage with threshold filter applied.

Results and Discussion

Comparing *before* and *after* states, we can conclude that the monoclinic twins do not change after the single passage of the single type II twin boundary. If any change occurred, it was not detectable by optical microscope. This indicates very high compatibility between monoclinic twins and type II twin boundary. To distinguish detailed changes, other microscopic techniques as for example SEM might be used. However, after many passages the monoclinic twins are affected significantly (not shown here).

Monoclinic twins on opposite sides (A and B) are identical at least in optical microscopy scale. The side B pictures are flipped vertically for direct comparison (marked by F letter). The identical monoclinic patterns indicate that the twin boundaries occupy macroscopic planes and propagate through the whole sample. Although the observation is only from the surface, it is implausible that the twins in the bulk are not planar. This is in agreement with the model [2, 3] in which monoclinic twins lie in the (010) plane.
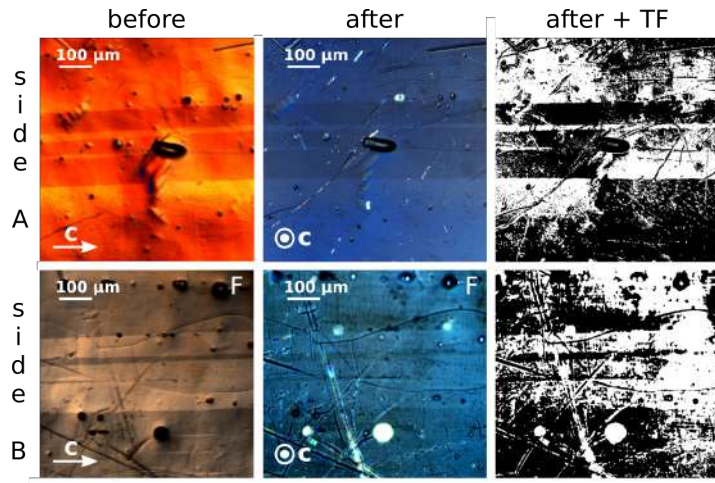
Figure 1: The optical micrographs of monoclinic twinning. Pictures were taken from side A and B *before* and *after* single type II twin boundary passed. The state *before* was taken with Nomarski contrast and *after* with polarization contrast. In addition, threshold filter (TF) was applied on polarization contrast pictures in order to increase their contrast. The side B pictures were flipped vertically to allow direct comparison (marked by F letter).

Conclusions

We showed that the monoclinic twinning boundaries are planar and macroscopic. In addition, any change of monoclinic twins by few passages of single type II boundary is not detectable by optical microscope. However, SEM technique might show differences after the passage. Nevertheless, the main question, whether monoclinic twins affect twinning stress of type II twin boundary, still remains.

References

[1] K. Ullakko, J. K. Huang, C. Kanter, V. V. Kokorin, R. C. O'Handley. Large magnetic-field-induced strains in Ni_2MnGa single crystals. *Appl Phys Lett* **69**(13): 1966, 1996.

[2] L. Straka, O. Heczko, H. Seiner, N. Lanska, J. Drahokoupil, A. Soroka, S. Fähler, et al. Highly mobile twinned interface in 10M modulated Ni-Mn-Ga martensite: Analysis beyond the tetragonal approximation of lattice. *Acta Mater* **59**(20): 7450, 2011.

[3] H. Seiner, L. Straka, O. Heczko. A microstructural model of motion of macro-twin interfaces in Ni-Mn-Ga 10M martensite. *J Mech Phys Solids* **64**: 198–211, 2014.

[4] O. Heczko. Magnetic shape memory effect and highly mobile twin boundaries. *Mater Sci Technol* **30**(13a): 1559–1578, 2014.

[5] O. Heczko, L. Klimša, J. Kopeček. Direct observation of a-b twin laminate in monoclinic five-layered martensite of Ni-Mn-Ga magnetic shape memory single crystal. *Scripta Materialia* **131**: 76–79, 2017.

Program pro analýzu jednotlivých difrakcí

Petr Veřtát[1,2], Jan Drahokoupil[3], Oleg Heczko[2]

[1]Katedra inženýrství pevných látek, Fakulta jaderná a fyzikálně inženýrská, České vysoké učení technické v Praze
[2]Oddělení magnetických měření a materiálů, Fyzikální ústav, Akademie věd České republiky
[3]Oddělení materiálové analýzy, Fyzikální ústav, Akademie věd České republiky
vertat@fzu.cz

Abstrakt

K získání přesných výsledků za pomoci rentgenové difrakce je zapotřebí důsledné a korektní analýzy jednotlivých difrakčních maxim. Pro tento účel jsme vytvořili a dále vyvíjíme jednoduchý a uživatelsky přívětivý program pro fitování difrakčních profilů. Program nabízí volbu v difraktometrii nejčastěji užívaných analytických funkcí (včetně asymetrických), umožňuje fixování libovolné kombinace parametrů, napomáhá rozlišení překrývajících se reflexí a je připraven k užití při řešení nejrůznějších problémů.

Klíčová slova: Rentgenová difrakce; Fitování difrakčních profilů; Asymetrie.

Úvod

Rentgenová difrakční analýza umožňuje na základě interakce fotonů rentgenového záření s atomy umístěnými v krystalové mříži vyšetřovat strukturu a složení zkoumané látky. Pozorujeme-li ve vhodném experimentálním uspořádání difrakci fotonů charakteristického rentgenového záření na krystalografické rovině *hkl*, jsme schopni, na základě známé Braggovy rovnice

$$\lambda = 2d_{hkl} \sin\theta, \tag{1}$$

kde λ značí vlnovou délku užitého záření a θ Braggův úhel, určit mezirovinnou vzdálenost d_{hkl}. Prvotním problémem při zkoumání monokrystalických vzorků je určení základní buňky, kdy na základě měření mezirovinných vzdáleností několika *hkl* rovin po aplikaci patřičných vztahů pro konkrétní krystalovou soustavu jsme schopni vypočítat mřížkové parametry. Mimo studium monokrystalů skýtá rentgenová difrakce mnohé další důležité aplikace, jmenujme například stanovení fázového složení či studium zbytkových napětí v měřeném vzorku, umožňující pokročilé studium pevných látek. [1] Naprostým základem při studiu materiálů pomocí rentgenové difrakce je však vždy pečlivá analýza jednotlivých naměřených reflexí, získaných většinou ve formě jednodimenzionálních záznamů. Pro tuto vyvíjíme vlastní vyhodnocovací program založený na prostředí *MS Excel* s makry v jazyce *VBA*. Tento náš program umožňuje uživatelsky přívětivé fitování jednotlivých difrakčních linií.

Fitování difrakčních profilů

Po proceduře načtení naměřených $I(2\theta)$ záznamů z několika nejužívanějších typů souborů (*.xrdml*, *.xy*, *.xye*) umožňuje program pomocí metody nejmenších čtverců na základě odpovídajícího spektra rentgenového záření fitovat vybrané profily některou z analytických funkcí uvedených v Tabulce 1 a tím podává podklad k další analýze.

Program umožňuje fitování několika linií najednou, což je mimořádně vhodné pro rozlišení překrývajících se reflexí, dále provádí upřesňování pozadí, poskytuje možnost fixování

libovolné kombinace parametrů během fitovací procedury či automatizaci celého procesu pro vyhodnocení vícera podobných měření.

Tabulka 1: Analytické funkce užívané při fitování difrakčních profilů. Parametr A_1 představuje intensitu reflexe, A_2 difrakční úhel, A_3 relativní šířku difrakční linie a A_4 tvarový parametr. [2]

Cauchy (Lorentz)	$f(x) = A_1 / (1+A_3(x-A_2)^2) = C(x)$
Gauss	$f(x) = A_1 \exp[A_3(x-A_2)^2] = G(x)$
Pearson VII	$f(x) = A_1 / (1+A_3(x-A_2)^2)^{A_4}$
Pseudo-Voigt	$f(x) = A_4 G(x) + (1-A_4) C(x)$

Problematickou může být situace, kdy z důvodů přístrojových, geometrických či jiných nevystihují zmíněné symetrické funkce z Tabulky 1 naměřený záznam dostatečně přesně. Pro fitování asymetrických profilů bylo přistoupeno k implementaci asymetrických funkcí založených na principu rozdílných parametrů tvaru a šířky pro obě poloviny difrakční linie [3].

Experiment

Příkladem pokročilého fitování naším programem, kde bylo přistoupeno k užití asymetrické funkce, je situace nastíněná na Obrázku 1. Reflexe -2 6 0 monokrystalu Ni-Mn-Ga byla měřena na difraktometru PANalytical Empyrean s vysokým rozlišením a monochromatickým svazkem. Naměřené body byly proloženy asymetrickou pseudo-Voigtovou funkcí s rozdílnými parametry pro levou a pravou stranu difrakční linie.
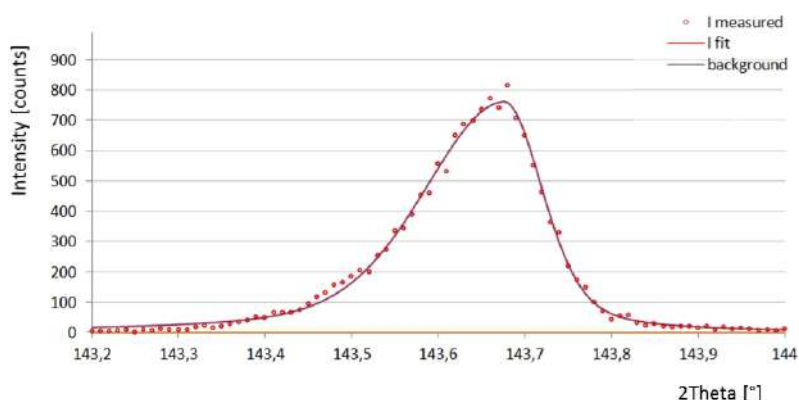
Obrázek 1: Silně asymetrický profil popsaný jednou silně asymetrickou funkcí.

Jak vidno, proložení bodů jediným silně asymetrickým profilem dává relativně dobrou shodu mezi naměřenými a vypočítanými daty. Problém asymetrické difrakční linie byl tedy užitím vhodné funkce v našem programu vyřešen.

Následný detailní rozbor situace na základě analýzy dvourozměrné mapy reciprokého prostoru s přihlédnutím k silné misorientaci vzorku však vede k interpretaci poněkud jiné – daná asymetrie je dána současným přispěním tří reflexí ve 2D mapě rozpoznatelných a oddělených (Obrázek 2). Při omezení se na jednodimenzionální záznam se pak tyto tři reflexe složí do jednoho silně asymetrického profilu. Korektní intepretaci na základě poznatků ze 2D mapy nastiňuje Obrázek 3. Vidíme, že program ani s takovouto situací nemá problém a dobře poslouží k nafitování odhalených překrývajících se tří linií – příspěvků od jednotlivých bodů v 2D mapě.
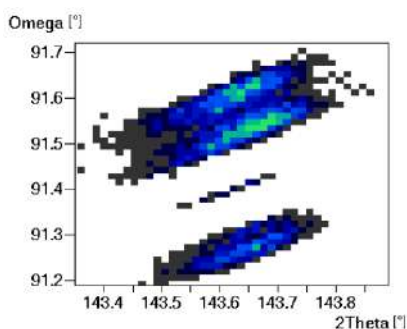
Obrázek 2: Dvoudimenzionální 2θ-ω mapa reflexe rozpadlé z důvodu misorientace.
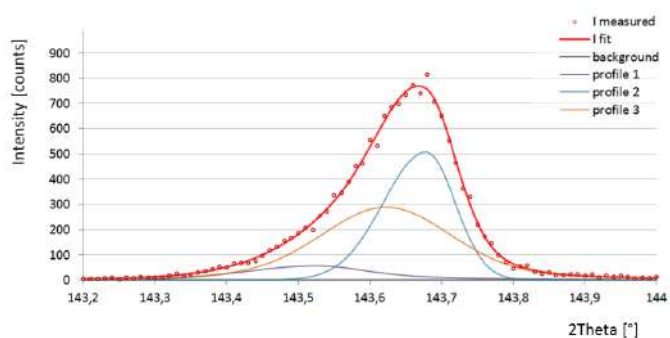
Obrázek 3: Silně asymetrický profil řádně popsaný třemi mírně asymetrickými příspěvky.

Závěr

Nastínili jsme problematiku analýzy jednotlivých difrakčních profilů pomocí našeho snadno přístupného fitovacího programu založeného na platformě *MS Excel* a *VBA*. Tento již doznal aplikací na několika pracovištích, zejména na poli analýzy monokrystalových reflexí či analýzy zbytkových napětí. Demonstrovali jsme jednu z možností programu - fitování silně asymetrické reflexe složené z několika příspěvků. V případě zájmu o kopii programu k využití pro svůj výzkum nechť čtenář laskavě kontaktuje autora (vertat@fzu.cz). ☺

Reference

[1] I. Kraus. *Úvod do strukturní rentgenografie*. Academia, 1985.

[2] R. Kužel. Informace v práškovém difraktogramu a jeho zpracování. *Materials Structure* **10**(1a): 18–19, 2003.

[3] H. Toraya. Whole-Powder-Pattern Fitting Without Reference to a Structural Model: Application to X-ray Powder Diffractometer Data. *J App Cryst* **19**: 440–447, 1986.

Spark Plasma Sintering of a High Entropy Alloy

Martin Dudr[1,2], František Lukáč[2], Radek Mušálek[2], Monika Vilémová[2], Jakub Cinert[2], Jakub Klečka[2]

[1]Czech Technical University in Prague, Faculty of Nuclear Sciences and Physical Engineering, Trojanova 13, Prague 2, 120 00, Czech Republic
[2]Institute of Plasma Physics, Czech Academy of Science, Za Slovankou 3, 182 00 Prague, Czech Republic
martin.dudr@gmx.com

Abstract

High entropy alloy HfNbTaTiZr was attempted to prepare by means of mechanical alloying followed by spark plasma sintering (SPS). W-rich inclusions and unmilled powder were discovered in the powder milled from pure metal powders in planetary ball mill with WC components. Spark Plasma Sintering of this powder carried out at temperature of 650°C resulted in poor compaction, hence higher sintering temperatures are recommended. Suggestion for optimised milling parameters was made.

Keywords: High entropy alloy; HfNbTaTiZr; SPS; Mechanical alloying.

Introduction

High Entropy Alloys (HEAs) are multicomponent alloys defined by being comprised of at least five elements in equiatomic or near-equiatomic ratios (that is usually interpreted as a range of 5-35 at.% per element). High configurational entropy of these alloys may enhance the formation of one equilibrium phase as solid solution with randomly distributed atoms occupying lattice points of usually BCC or FCC structure.

The special nature of these alloys allows them to have remarkable properties like high hardness, stability of phase composition, creep resistance, radiation resistance, low diffusion coefficient, biocompatibility and others.

The Hf-Nb-Ta-Ti-Zr alloy (HfNbTaTiZr) has been developed as a refractory alloy by Senkov in 2011 [1]. It is also considered as a potential biocompatible material [2]. It forms a single phase BCC solid solution at RT.

Experimental

All manipulations with powders (milling vessel filling, depositing and SPS die loading) were carried out under protective argon atmosphere (in glove box) in order to suppress formation of oxide layer.

A mixture of powders of pure metals Hf-Nb-Ta-Ti-Zr with 99.9% purity in equi-atomic ratio was mechanically alloyed (MA) in a planetary ball mill Pulverisette 5 (Fritsch, Germany) equipped with WC components. The milling was carried out under argon atmosphere and at 230 RPM with ball-to-powder ratio 10:1 for 36 hours.

The milled powder was subsequently wrapped in tungsten foil and compacted in the spark plasma sintering device FCT SPS-HP25 using graphite die and punches. Powder was sintered at 650°C with no holding time (i.e. heating was terminated just after reaching the temperature) and under the load of 100 MPa. Samples were sintered in a form of cylinders of a diameter of 20 mm and the remains of tungsten foil after sintering process were removed by grinding.

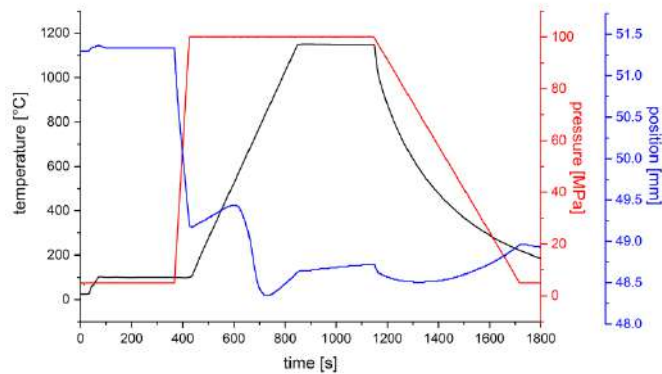The sintering process commences at temperature 600°C, as indicated in Figure 1.

Figure 1: The time dependence of temperature (black), measured pressure (red) and relative position of punches (blue). Drop in punches position around 600 s of experiment time marks the initiation of sintering process. This sample was sintered at 1150°C for 5 minutes under 100 MPa.

Scanning electron microscope EVO MA 15 (Carl Zeiss SMT, Oberkochen, Germany) in backscattered mode and equipped with EDS detector XFlash® 5010 (Bruker, Karlsruhe, Germany) was used to characterize microstructural morphology of both the powder and the sintered sample.

XRD measurements were carried out at Bruker D8 Discover diffractometer (Bruker, Karlsruhe, Germany) in Bragg-Brentano geometry with divergent beam using CuK_{α} radiation, Ni β-filter in front of 1D LynxEye detector (Bruker, Karlsruhe, Germany). Rietveld refinement was performed in TOPAS 5 (Bruker, Karlsruhe, Germany) [3].

Results and discussion

SEM close-up images of the free milled powder and of the sintered sample are in Figure 2.
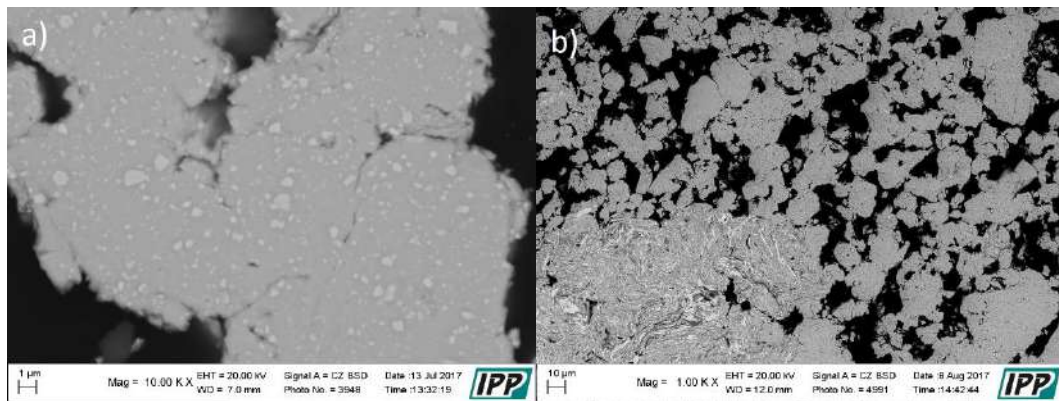
Figure 2 SEM images of the a) milled powder and b) SPS sample.

The image of powder a) reveals a number of evenly distributed light inclusions in otherwise homogenous matrix. EDS analysis showed that these inclusions are W-rich, probably they are WC fragments from the mill components (balls and vessel). Non-homogenous particles were also observed in the free powder, similar ones like that in Figure 2 b). These were not milled thoroughly and using EDS there were observed regions of different pure metals in one particle.

SEM image of the SPS sample on the right in Figure 2 was taken close to the edge of the sample, where the porosity was greater, however generally it is concluded that the sintering temperature needs to be higher than 650°C in order to achieve good compaction. WC inclusions were preserved after sintering and they were not found in the unmilled regions.

Rietveld refinement was carried out at XRD pattern of the SPS sample, results being displayed in Figure 3. Phase composition was determined to be (in descending order): a BCC structure with a lattice parameter a = 3.3388(1) Å, a hexagonal phase with lattice parameters very close to hexagonal Hf, tungsten carbide and pure tungsten (remains of the foil). Amounts of W and WC are in units of wt%, BCC content is 2-3 times higher than the content of hexagonal phase.
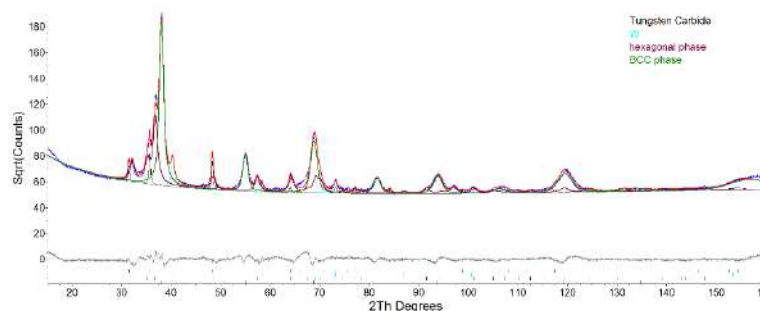
Figure 3: Rietveld refinement of XRD measurement on the sample sintered at 650°C.

Conclusion

Powders of pure metals Hf, Nb, Ta, Ti and Zr were high-energy-ball milled in a WC-component-equipped planetary mill and the milled powder was subsequently sintered using SPS method at 650°C.

The XRD showed that mechanical alloying of pure powders was initiated. However, milled powder contains unmilled particles of the original metals and some W-rich inclusions, probably WC from the milling components.

It is concluded that the sintering occurs at a temperature relatively low in comparison to the melting temperature. Spark plasma sintering of milled powder at 650°C was sufficient for partial compaction with some porosity, however higher temperatures are needed to enhance the diffusion rate and eliminate the porosity completely.

References

[1] O.N. Senkov, J.M. Scott, S.V. Senkova, D.B. Miracle, C.F. Woodward. *J of Alloy Compd* **509**(20): 6043–48, 2011.
[2] V. Braic, M. Balaceanu, M. Braic, A. Vladescu, S. Panseri, A. Russo. *J Mech Behav Biomed Mater* **10**:197-205, 2012.
[3] A.A Coelho. TOPAS, version 5 (Computer Software); Coelho Software: Brisbane, Australia, 2016.

Anisotropic Elastic and Acoustic Properties of Robocast Silicon Carbide Scaffolds

Martin Koller[1], Alena Kruisová[2], Hanuš Seiner[2], Petr Sedlák[2],
Michal Landa[2], Benito Román-Manso[3], Manuel Belmonte[4], Pilar Miranzo[4]

[1]Department of Materials, Faculty of Nuclear Sciences and Physical Engineering, Czech Technical University in Prague
[2]Institute of Thermomechanics, Czech Academy of Sciences, Prague
[3]School of Engineering and Applied Sciences, Harvard University
[4]Institute of Ceramics and Glass (ICV-CSIC), Madrid
martin.koller@fjfi.cvut.cz

Abstract

Robocasting is an additive manufacturing technique for fabricating ceramic scaffolds composed of thin ceramic rods. Ceramic green bodies are obtained by extruding a ceramic-based viscous ink following a layer-by-layer printing route, and the scaffolds are then consolidated by pressureless spark plasma sintering. It is shown how the macroscopic periodic structures of silicon carbide scaffolds affect acoustic properties, depending on material symmetries given by the scaffolds geometry. In the low-frequency limit, a strong acoustic energy focusing along the ceramic rods is observed for tetragonal and orthorhombic symmetries, while the hexagonal samples are isotropic in the hexagonal plane.

Keywords: Ceramic scaffolds; Robocasting; Acoustic energy focusing.

Introduction

The use of additive manufacturing (AM) techniques has grown rapidly in recent years, as these methods are capable of fabricating complex structures by layer-by-layer deposition. Robocasting is an AM method, in which the ceramic micro-architectured scaffolds consisting of thin ceramic rods are produced. Such scaffolds exhibit unique acoustic and elastic properties, such as strong elastic anisotropy [1], or frequency band gaps in MHz-range [2]. In this contribution, several types of silicon carbide robocast structures were used as templates for finite element modeling of their anisotropic acoustic properties, where acoustic energy focusing along the ceramic rods is observed.

Materials and Methods

The fabrication of robocast silicon carbide scaffolds consisted of several particular steps [3]. SiC-based powder (80 wt. % of β-SiC with sintering additives of Al_2O_3 and Y_2O_3) was dispersed in aqueous polymer solution, and mixed with methylcellulose viscosifying agent and ammonium polyacrylate flocculant. This colloidal gel ink was then extruded through a nozzle onto an alumina substrate in an oil bath at room temperature, following a printing route defined by computer-aided design (CAD). After drying at room temperature, the organic additives were burnt out at 600 °C for 2 hours. Finally, the ceramic compacts were sintered by pressureless spark plasma sintering at 1700 °C for 5 minutes.

Six types of robocast SiC scaffolds were studied, exhibiting three types of material symmetry. In each sample, the ceramic rods have parallel orientations with equidistant in-plane spacings between the rods and the samples differ in mutual orientation of neighbouring layers.

Elastic and acoustic properties of the scaffolds were calculated by finite element modeling in COMSOL Multiphysics software. The geometric parameters of each studied scaffold were measured from the sintered samples, and SiC material properties were implemented into the calculations. For each sample, a computational unit was designed and the elastic coefficients were obtained by applying tensile or shear straining modes. Finally, group velocity distributions were computed from the full set of elastic coefficients.

Results and Discussion

Group velocity distributions of robocast SiC scaffolds, as computed by finite element modeling, are shown in Fig. 1 and Fig. 2. The group velocity values are plotted as single points in order to demonstrate acoustic energy focusing. The outer red-colored points represent quasi-longitudinal wave and the blue-colored points represent two quasi-transverse waves; there are 360 points for each type of wave in the group velocity plots.
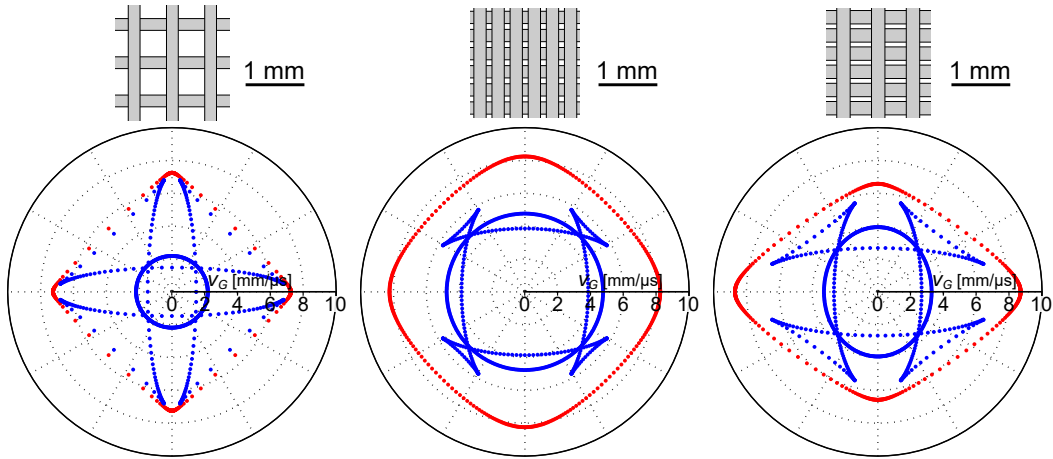
Figure 1: Group velocity distributions for the scaffolds with perpendicular orientation of neighbouring layers.

As seen in Fig. 1 for the samples with perpendicular orientations of the ceramic rods, acoustic energy is focused mainly along the rods. The level of energy focusing depends on the scaffolds geometry; if there is a higher in-plane spacing between the rods, the energy is more focused along the rods. With decreasing in-plane spacings, the energy is still focused along the rods, but it is less pronounced, as seen in the comparison of the tetragonal samples in Fig. 1. For the sample with two different in-plane spacings between the rods, it can be seen that the group velocity in the principal axes is higher in the direction with denser arrangement of the ceramic rods.

Different situation can be observed for the scaffolds in Fig. 2. For the orthorhombic scaffold with the 46° angle between the rods, the acoustic energy is slightly focused along all directions within this angle.
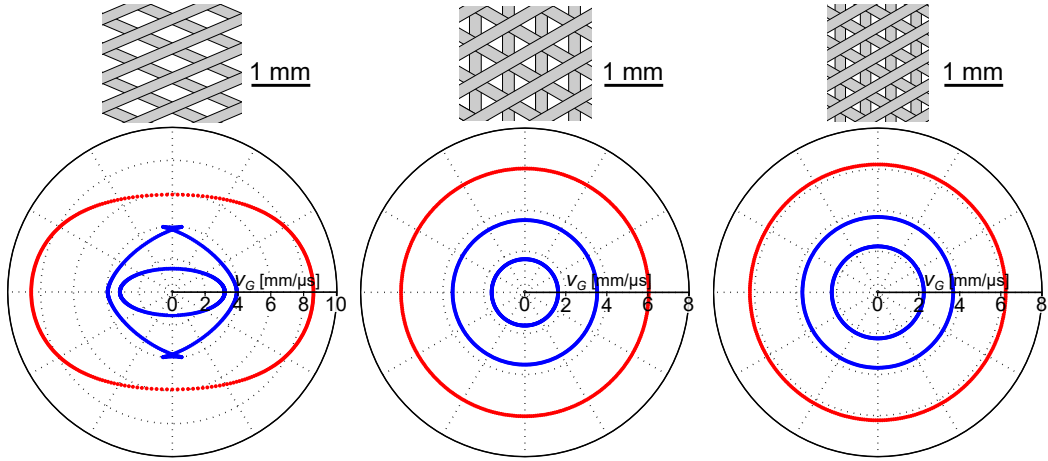
45

Figure 2: Group velocity distributions for the scaffold with 46° angle between rods of neighbouring layers and for hexagonal scaffolds.

The hexagonal scaffolds exhibit in-plane isotropy due to the highest material symmetry among the studied scaffolds. Nevertheless, the acoustic properties of the hexagonal scaffolds were determined under the condition of macroscopic homogeneous material in the low-frequency limit where the wavelengths of the acoustic waves are much higher than the principal dimensions of the scaffolds. When the wavelengths become comparable to the in-plane spacing of the rods, some acoustic energy focusing along the rods can be expected even in the hexagonal scaffolds, as will be shown elsewhere.

Conclusions

Anisotropic acoustic properties of robocast SiC scaffolds were determined from full set of elastic coefficients calculated by finite element modeling. It was shown that the acoustic energy is focused along the ceramic rods in the tetragonal and orthorhombic samples, where the geometry of the scaffolds plays crucial role in the energy focusing. On the other hand, the hexagonal scaffolds are in-plane isotropic if the wavelengths of acoustic waves are much higher than the principal dimensions of the scaffolds.

References

[1] A. Kruisová, et al. Acoustic metamaterial behavior of three-dimensional periodic architectures assembled by robocasting. *Appl Phys Lett* **105**: 211904, 2014.

[2] A. Kruisová, et al. Ultrasonic bandgaps in 3D-printed periodic ceramic microlattices. *Ultrasonics* **82**: 91–100, 2018.

[3] K. Cai, et al. Geometrically Complex Silicon Carbide Structures Fabricated by Robocasting. *J Am Ceram Soc* **95**: 2660–2666, 2012.

Spektroskopické studie bilirubin oxidázy a jejího mutantu

Leona Švecová[1,2], **Tomáš Koval'**[2], **Tereza Skálová**[2], **Lars Henrik Østergaard**[3], **Jan Dohnálek**[2]

[1]Katedra inženýrství pevných látek, Fakulta jaderná a fyzikálně inženýrská, České vysoké učení technické v Praze, Břehová 7, 115 19, Praha 1
[2]Biotechnologický ústav Akademie věd ČR, centrum Biocev, Průmyslová 595, 252 50 Vestec, Česká republika
[3]Novozymes A/S, Brudelysvej 26, DK-2880 Bagsvaerd, Dánsko

Abstract

Bilirubin oxidáza (BOD) z organismu *Myrothecium verrucaria* je využívána v medicíně pro stanovení množství bilirubinu v krvi při vyšetření jater. Přestože byla krystalová struktura BOD již publikována dříve, neodpovídá na otázku týkající se určení aminokyselin účastnících se přenosu e⁻ od e⁻- poskytujícího substrátu k primárnímu akceptoru e⁻. Pro zodpovězení této otázky byl navržen a připraven mutant BOD s lokální mutací aminokyseliny v blízkosti aktivního místa BOD. Spektroskopické studie ukázaly, že navzdory mutaci, zůstala struktura a stabilita vzorku zachována.

Klíčová slova: Bilirubin oxidáza; Cirkulární dichroismus.

Úvod

Bilirubin oxidáza z rostlinného patogenu *Myrothecium verrucaria* (BOD; EC 1.3.3.5) je schopná katalýzy oxidace širokého spektra organických a některých anorganických látek doprovázené redukcí molekulárního kyslíku na vodu. BOD je známá především díky katalýze oxidace bilirubinu na biliverdin, čehož je využíváno v medicíně při stanovení množství bilirubinu v krvi při vyšetření jater [1].

BOD obsahuje 4 redoxně aktivní ionty mědi v aktivních místech. Tyto ionty Cu jsou děleny na tři typy podle jejich spektroskopických a magnetických vlastností. BOD má celkem dvě aktivní místa - *oxidační* a *redukční*. Oxidační místo obsahuje iont Cu typu I (T1), který je primárním akceptorem elektronů od e⁻-poskytující látky. Od T1 jsou e⁻ transportovány přes cystein-histidinové můstky do redukčního aktivního místa, které obsahuje iont Cu typu II (T2) a 2 ionty Cu typu III (T3). Redukční místo je zodpovědné za redukci O_2 na H_2O [2].

Přestože byla krystalová struktura BOD již vyřešena a popsána dříve (PDB kód: 2XLL [1], 3ABG [3]), stále zde zůstávají nezodpovězené otázky týkající se mechanismu vazby substrátu a cesty transportu e⁻ od e⁻-poskytující látky k T1. S cílem přiblížit se odpovědím na tyto otázky byl navržen mutant s lokální mutací aminokyseliny v blízkosti oxidačního aktivního místa. Tato práce se zabývá stanovením vlivu mutace na výsledný vzorek a vhodností vzorku pro další studie.

Experiment

Cirkulární dichroismus (CD)

Zachování terciární struktury mutantu (mBOD) enzymu BOD bylo studováno pomocí *CD absorpční spektroskopie*. Bylo stanoveno procentuální zastoupení prvků sekundární

struktury a ověřena přítomnost iontů Cu (T1 a T3) v aktivních místech BOD a mBOD. Pro studium terciární struktury bylo použito UV záření o vlnových délkách 186-260 nm a pro ověření přítomnosti kovů záření o vlnových délkách 300-800 nm. Vzorky enzymů byly rozpuštěny v roztoku obsahujícím 20 mM fosfátový pufr pH 7,4 a 100 mM NaCl a jejich koncentrace byla 0,1 mg/ml pro měření v UV oblasti a 3,5 mg/ml v UV/VIS oblasti záření.

Výsledky a diskuze

Změny ve struktuře mutantu mBOD oproti nemutovanému enzymu BOD byly studovány pomocí UV CD absorpční spektroskopie. Procentuální zastoupení prvků sekundární struktury shrnuje tabulka 1. Z výsledků je patrné, že při mutaci nedošlo v terciální struktuře k výrazným změnám. Přítomnost iontů mědi ve strukturách BOD a mBOD byla ověřena pomocí UV/VIS CD absorpční spektroskopie. V obou případech byl pozorován signál při 610 nm odpovídající absorpci iontem Cu T1 a dále signál při 330 nm odpovídající páru iontů Cu T3 spojených pomocí hydroxidového iontu OH^- [4]. CD absorpční spektra jsou uvedena na obrázku 1.
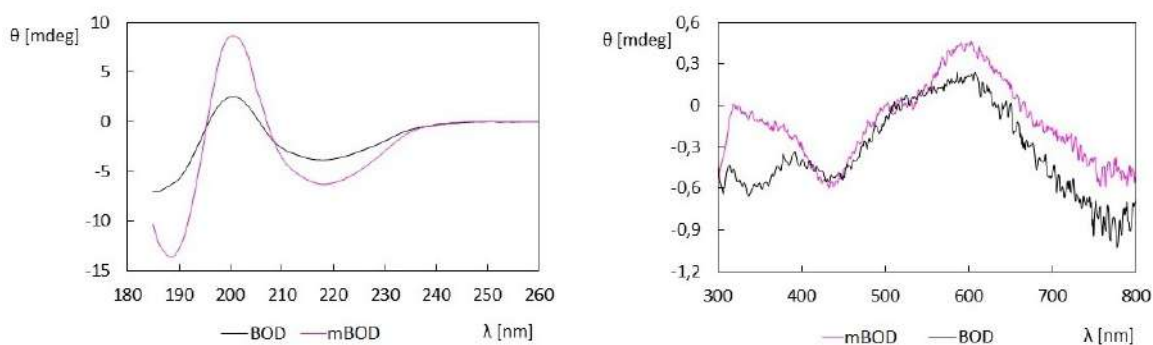
Obrázek 1: UV CD (vlevo) a UV/VIS CD (vpravo) absorpční spektrum BOD a mBOD.

Tabulka 1: Procentuální zastoupení prvků sekundární struktury BOD a mutantu mBOD stanovených pomocí UV CD absorpční spektroskopie.

	BOD	mBOD
α-šroubovice (%)	12,3	12,5
β-vlákno (%)	39,5	37,4
β-ohyb (%)	15,4	15,0
smyčka (%)	32,8	35,3

Závěr

Bilirubin oxidáza z rostlinného patogenu *Myrothecium verrucaria* (BOD) patří mezi více-měďné oxidoreduktázy, které využívají 4 redoxně aktivní ionty Cu kovalentně navázané ve

struktuře k přenosu e⁻ od e⁻-poskytující látky ke konečnému akceptoru e⁻ (O_2). Cesta transportu e⁻ přes ionty Cu byla podrobně studována a popsána. Nicméně cesta e⁻ od e⁻-poskytující látky k primárnímu iontu mědi (T1) dosud popsána nebyla.

S cílem objasnit tuto cestu byla navržena lokální mutace aminokyseliny (v blízkosti aktivního místa BOD), podezřelá z účasti na transportu e⁻. Zachování terciární struktury BOD a jejího mutantu mBOD a přítomnost iontů mědi byla ověřena pomocí CD absorpční spektroskopie. Experimentálně bylo prokázáno, že mutací nedošlo k významné změně struktury oproti nemutovanému enzymu. Na základě těchto výsledků lze doporučit vzorek mutantu k další analýze a ke studiu enzymatické aktivity, která by měla jeho roli při transportu e⁻ prokázat.

Reference

[1] J. A. Cracnell, et al. Bilirubin oxidase from *Myrothecium verrucaria*: X-ray determination of the complete crystal structure and a rational surface modification for enhanced electrocatalytic O_2 reduction. *Dalton Trans* **40**: 6668-6675, 2011.

[2] D. J. Kosman. Multicopper oxidases: a workshop on copper coordination chemistry, electron transfer, and metallophysiology. *J Biol Inorg Chem* **15**: 15-28, 2010.

[3] K. Mizutami, et al. X-ray analysis of bilirubin oxidase from *Myrothecium verrucaria* at 2.3 Å resolution using a twinned crystal. *Acta Cryst* **F66**: 765-770, 2010.

[4] H. Morishita, et al. Study on dioxygen reduction by mutational modifications of the hydrogen bond network leading from bulk water to the trinuclear copper center in bilirubin oxidase. *Biochem Biophys Res Commun* **450**: 767-772, 2014.

Difrakční limit v makromolekulární krystalografii

Martin Malý[1,2], **Jarmila Dušková**[2], **Lars Henrik Østergaard**[3], **Jan Stránský**[1,2], **Leona Švecová**[1,2], **Petr Kolenko**[1,2], **Jan Dohnálek**[2]

[1]Katedra inženýrství pevných látek, Fakulta jaderná a fyzikálně inženýrská, České vysoké učení technické v Praze, Břehová 7, 115 19, Praha 1, Česká republika
[2]Biotechnologický ústav AV ČR, v. v. i., BIOCEV, Průmyslová 595, 252 50, Vestec, Česká republika
[3] Novozymes A/S, Brudelysvej 26, DK-2880 Bagsvaerd, Dánsko
malymar9@fjfi.cvut.cz

Abstrakt

Difrakční limit pro vysoké rozlišení je jedním z důležitých parametrů, které je třeba vhodně zvolit při řešení makromolekulární struktury. Na testovací soubor difrakčních dat z proteinového krystalu byla aplikována různá kritéria volby difrakčního limitu. Následně byl zanalyzován jejich dopad na mapy elektronové hustoty, výslednou strukturu a její statistiky. Důraz byl kladen především na metodiku tzv. párového upřesňování – analýzu statistik upřesňování R_{work} and R_{free}.

Klíčová slova: Rentgenová strukturní analýza; Difrakce; Difrakční limit.

Úvod

Intenzita reflexí pozorovaných na difrakčních snímcích obecně klesá s rostoucím rozlišením. V oblasti vysokého rozlišení proto data obvykle obsahují už jen velmi málo užitečného signálu a naopak jsou výrazně zatížena šumem. Při zpracování difrakčních dat je tedy nutné stanovit difrakční limit pro vysoké rozlišení – hodnotu rozlišení, do kterého budou data zpracována; zbylá data nebudou použita.

Pro určení difrakčního limitu je třeba kvalitu dat kvantifikovat. Mezi nejpoužívanější statistiky patří R-faktory R_{merge} a R_{meas}, poměr signálu ku šumu I/σ a korelační koeficient $CC_{1/2}$. Tyto indikátory kvality jsou však bez vztahu ke strukturnímu modelu. Dále je diskutabilní, které jejich hodnoty jsou ještě přípustné pro použitelná data.

Po zpracování dat a vyřešení fázového problému je možné ověřit volbu difrakčního limitu pomocí analýzy R-faktorů R_{work} a R_{free} v průběhu procesu upřesňování struktury [1]. Tyto statistiky jsou vztaženy k aktuálnímu strukturnímu modelu a jejich současný pokles (případně pokles pouze R_{free}) značí vylepšení modelu. Tento postup bude demonstrován na testovacích datech struktury enzymu s ligandem.

Experiment

Difrakční data byla získána na synchrotronu Petra III v Hamburku (stanoviště P13). Vzdálenost vzorek-detektor byla 419,67 mm, další parametry experimentu byly: $\Delta\phi = 0{,}1°$; $\Delta t = 0,15$ s; $\phi_{total} = 200°$. Difrakční data byla zpracována pomocí programu XDS [2].
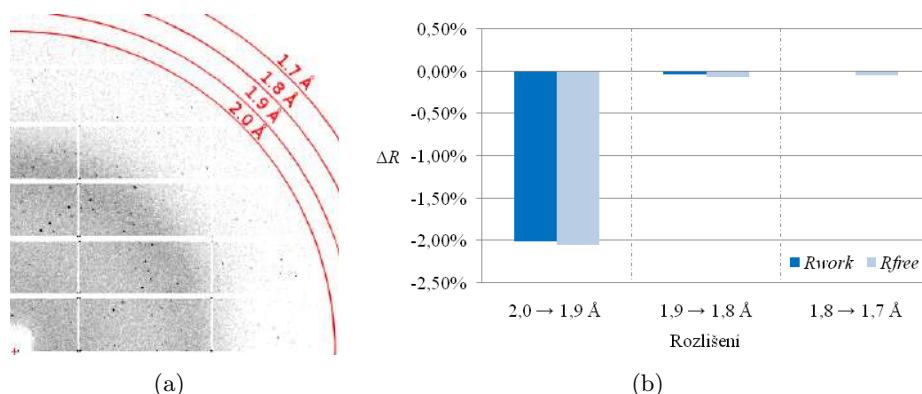
Obrázek 1: (a) Vybraná část difrakčního snímku krystalu enzymu s vyznačenými slupkami s vysokým rozlišením. (b) Pokles hodnot R-faktorů R_{work} a R_{free} příslušných k zvoleným difrakčním limitům. ΔR je hodnota rozdílu hodnot R-faktoru nižšího a vyššího rozlišení.

Výsledky

Reflexe byly při vizuální inspekci spatřeny do rozlišení 2,2 Å. Při stanovení parametru průměrného $I/\sigma \geq 2$ pro vrstvu reflexí s nejvyšším rozlišením byl difrakční limit stanoven na 2,0 Å.

Fázový problém byl vyřešen metodou molekulárního nahrazení za použití struktury téhož enzymu – PDB kód 3RJ8 [3]. Model byl upřesněn pomocí programu Refmac5 [4].

Před modelováním ligandů byla do procesu upřesňování struktury postupně přidávána data ze slupek 2,0–1,9 Å; 1,9–1,8 Å a 1,8–1,7 Å (Obr. 1(a)). Po přidání každé slupky byl strukturní model upřesněn (20 cyklů) a současně byly porovnány R-faktory na stejné hladině rozlišení (Obr. 1(b)). K významnému snížení hodnot obou R-faktorů došlo pouze po přidání dat ze slupky 2,0–1,9 Å. Difrakční limit pro vysoké rozlišení byl tedy na základě této analýzy změněn na 1,9 Å.

Tabulka 1: Statistické výsledky zpracování a upřesňování. Hodnoty v závorkách odpovídají slupce s nejvyšším rozlišením.

Vlnová délka [Å]	0,9201	Počet upřesňovaných atomů	4 350
Prostorová grupa	$C121$	Počet upřesňovaných molekul vody	521
Elem. buňka [Å, °]	$a = 132{,}77$; $b = 56{,}99$;	Průměrný ADP	31
	$c = 86{,}88$; $\beta = 95{,}66$;	$Rms\ bond$ [Å]	0,010
	$\alpha = \gamma = 90{,}00$	$Rms\ angle$ [°]	1,415
Difrakční limit [Å]	50,00–1,90 (2,01–1,90)	R_{free} (5 %)	0,213
Počet reflexí	135 014 (18 160)	R_{work} (95 %)	0,173
Počet nez. reflexí	48 682 (7 325)	Ramach.: povolené konformace [%]	100
R_{merge}	0,101 (1,013)	Ramach.: zakázané konformace [%]	0
R_{meas}	0,122 (1,251)		
$CC_{1/2}$	0,995 (0,354)		
I/σ [I]	7,9 (1,3)		
Redundance	2,8 (2,5)		
Kompletnost [%]	94,9 (89,5)		

Diskuze

Díky analýze R-faktorů byla použita i data ze slupky o rozlišení 2,0–1,9 Å, která byla původně podle konzervativního kritéria pro I/σ vyloučena. Tato slupka však obsahuje 15 % nezávislých reflexí (Tab. 1). Data z vysokého rozlišení navíc obsahují informace o strukturních detailech. V důsledku použití dat z této slupky došlo k vylepšení strukturního modelu, což bylo zejména patrné na elektronové hustotě molekuly ligandu (Obr. 2).

(a) (b)
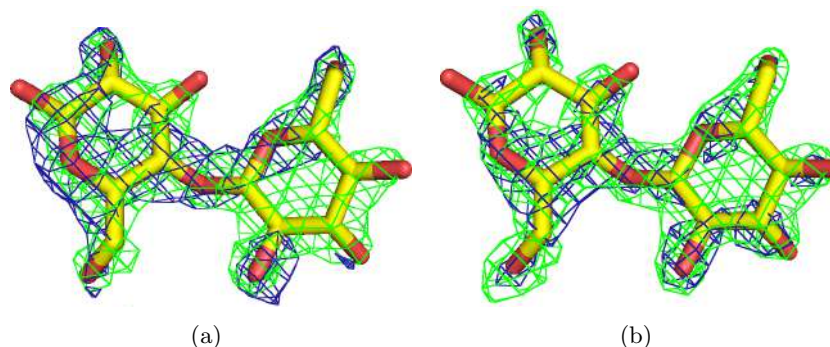
Obrázek 2: Mapy elektronové hustoty ligandu v aktivním místě enzymu. Modrá barva přísluší zpracování s difrakčním limitem 2,0 Å, zelená odpovídá optimalizovanému zpracování s difrakčním limitem 1,9 Å. (a) $2F_O - F_C$ mapy na hladině elektronové hustoty 1,5σ. (b) $F_O - F_C$ (diferenční) „omit" mapy na hladině elektronové hustoty 3,8σ.

Závěr

Difrakční limit je důležitý parametr zpracování difrakčních dat. Na modelovém příkladě byl demonstrován postup, jak zvolit difrakční limit pro vysoké rozlišení tak, aby byla použita všechna data obsahující užitečný signál. Byl pozorován pozitivní vliv této volby na podobu map elektronové hustoty, a tedy přímo na kvalitu strukturního modelu.

Reference

[1] P. A. Karplus, K. Diederichs. Linking Crystallographic Model and Data Quality. *Science* **336**: 1030–1033, 2012.

[2] W. Kabsch. XDS. *Acta Cryst. D***66**: 125–132, 2010.

[3] J. Dušková, T. Skálová, A. Štěpánková, T. Kovaľ, J. Hašek, L. H. Østergaard, C. C. Fuglsang, P. Kolenko, J. Dohnálek. PDB ID: 3RJ8. [2017-04-15]. `http://www.rcsb.org/pdb/explore/explore.do?structureId=3RJ8`. 2011.

[4] G. N. Murshudov, A. A. Vagin, E. J. Dodson. Refinement of Macromolecular Structures by the Maximum-Likelihood Method. *Acta Cryst. D***53**: 240–255, 1997.

Luminescence Properties of InGaN/GaN Heterostructures

František Hájek[1,2], Alice Hospodková[2], Karla Kuldová[2], Jiří Oswald[2], Jiří Pangrác[2], Zdeněk Potůček[1]

[1]Department of Solid State Engineering, Faculty of Nuclear Sciences and Physical Engineering, Czech Technical University in Prague
[2]Semiconductor Department, Institute of Physics, Czech Academy of Sciences

Abstract

In this work we present our results of InGaN/GaN multiple-quantum wells development for fast scintillation application. Photoluminescence (including photoexcitation spectra) and cathodoluminescence (CL) measurements are shown and discussed. Origin of the bands in luminescence spectra is discussed, especially the unusual "green band" which arises probably because of a donor-acceptor recombination.

Keywords: Photoluminescence; Cathodoluminescene; Nitride semiconductors; Quantum wells; Blue shift.

Introduction

Gallium nitride-based optoelectronic devices (lasers, light-emitting diodes) are attracting much attention in present days. One reason is surprisingly high internal and external quantum efficiencies which can be achieved, in spite the fact that a spontaneous polarization effect of nitride wurtzite structure along with a piezoelectric polarization effect of nitride heterostructures cause large quantum-confined Stark effect (QCSE) [1], [2].

Luminescence spectra of InGaN/GaN quantum wells (QWs) usually consist of only one peak, which belongs to the QW levels recombination. However, sometimes a new band can arise, for example from impurity levels in band gap. In this paper, the origin of the unusual "green band" in the luminescence spectra is discussed.

Experimental details

The low-temperature GaN layer was grown by metal-organic vapour phase epitaxy on c-oriented sapphire substrate. Next, the high temperature buffer GaN layer was deposited. On the top of this structure, the superlattice consisting of ten to thirty narrow (1-2 nm) InGaN quantum wells and wide GaN barriers was grown. The structure was capped by 25nm thick GaN layer. Other growing parameters vary for different specimens and can be found in [3]. Series of specimens were grown to observe the luminescence properties dependence on growing parameters.

Photoluminescence emission (PL) spectra were measured using 375 nm laser as excitation source with the excitation density of 10 Wcm^{-2}, monochromator, GaAs photoamplifier and synchronous detector PAR5205. The intensity oscillations are caused by different refractive indexes of sapphire, GaN and air (Fabry–Pérot oscillations). CL spectra were recorded via XL30 ESEM TMP scanning electron microscope and GaAs photoamplifier. Excitation spectra were measured by mercury vapour lamp, double monochromator and GaAs photoamplifier. Excitation spectra are corrected for excitation source emission.
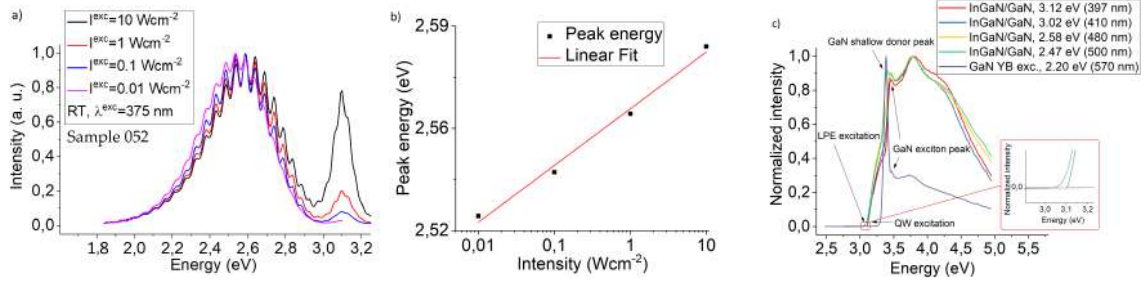
Figure 1: a) Typical PL spectrum at RT, b) LEP energy dependence on excitation density, c) Excitation spectra for GaN a InGaN/GaN QWs.

Results and discussion

Typical normalized PL spectrum measured at room temperature (RT) is shown in fig. 1a). The high energy peak belongs to QW recombination [2]. Its energy does not shift with increasing excitation density. The second low energy peak (LEP) undergoes the blue shift (with increasing excitation density it shifts to higher energies) at room temperature (fig. 1b)). For different specimens, the energy difference between the QW peak energy and LEP energy in PL spectra varies and no clear dependence on In content, growing temperature, *etc.* was observed except "synchronous" shift of the LEP energy with QW peak energy. Excitation spectra for typical sample are shown in fig. 1c). The red and blue lines are for excitation near QW band maximum, the yellow one is for the LEP at the wavelength, where we can exclude the influence of the notorious yellow band of GaN with maximum energy of 2.20 eV [4]. The energy difference between blue and yellow line is about 18 meV at energies around 3.1 eV.

First of all, the large blue shift (for different samples from 65 meV to 200 meV, when excitation density is increased by three orders) of the LEP has to be explained. One possibility is that this band arises because of In-rich quantum-dots-like structures (QDL) reported in some works [2], [5]. The blue shift would happen as a consequence of internal electric field screening (consequence of QCSE). However, if we assume normal distribution of In content in these QDL, the excitation spectra do not confirm this theory.

Another alternation could be donor-acceptor pairs (DAP) recombination. Carriers bounded at DAP are attracted with Coulombic interaction, which influences the recombination energy. Because this Coulombic interaction depends on distance r among excited centers as $\sim \frac{1}{r}$, the energy of recombination undergoes the blue shift. From available resources, to cause as high blue shift as 150 meV with three order excitation density increase, the concentration of responsible DAP should be at least of order $\sim 10^{18}$ cm^{-3} [4]. From the results of SIMS analysis, no such dopants are presented in our samples.

Next possibility is that the wide LEP is formed by more than just one peak and that the relative intensity of these peaks is changing with increasing excitation density. Thus, we fitted our PL spectra with Gaussian distributions, as can be seen in fig. 2a). With decreasing excitation density, the relative intensity of the QW peak decreases, on the other hand, intensity of the YB increases. The middle peak exhibits a blue shift, but smaller, usually under 90 meV. This shift could be caused by DAP recombination. In the fig. 2b) is depicted typical CL map for our InGaN/GaN QWs. The aim of this mapping was to determine correlation between QW luminescence and LEP luminescence. The CL map
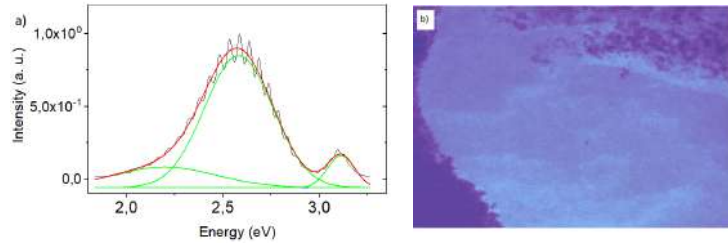
Figure 2: a) Gaussian fitting of PL spectra, b) CL mapping with color filters.

was measured twice, once with filter for QW emission and once with filter for LEP. The first measurement was transformed into shades of red, the second one into shades of blue. The overlap of these two emissions is given by the shades of purple. It is evident from these maps that the LEP is strong in the same sites as the QW emission. Thus, the most probable explanation for LEP is DAP recombination, where one of the levels (probably the donor one) is about 18 meV below the first QW energy level. However, no direct evidence for this conclusion is available yet and future research is needed.

Conclusion

In conclusion, we investigated the origin of unusual "green" luminescence band using PL emission and excitation spectra and CL mapping. From these results the DAP recombination was proposed as the most probable explanation for this luminescence band.

References

[1] Ch.-Y. Chang, et al. Manipulation of nanoscale V-pits to optimize internal quantum efficiency of InGaN multiple quantum wells. *Appl Phys Lett* **106**(9): 091104, 2015.

[2] G. Pozina, et al. Origin of multiple peak photoluminescence in InGaN/GaN multiple quantum wells. *J of Appl Phys* **88**(5): 2679, 2000.

[3] A. Hospodková, et al. On the correlations between the excitonic luminescence efficiency and the QW numbers in multiple InGaN/GaN QW structure. *J of Appl Phys* **121**(21): 214505, 2017.

[4] M. A. Reshchikov, H. Morkoç. Luminescence properties of defects in GaN. *J of Appl Phys* **97**(6): 061301, 2005.

[5] J. Y., L. Wang, et al. Improving the internal quantum efficiency of green InGaN quantum dots through coupled InGaN/GaN quantum well and quantum dot structure. *Appl Phys Expr* **8**(9): 09401, 2015.

Investigation of Silicon-Vacancy Centre Photoluminescence in CVD Diamond Thin Film Growth on Different Substrates

Kateřina Dragounová[1,2], Tibor Ižák[2], Zdeněk Potůček[1], Štěpán Potocký[2], Zdeněk Bryknar[1], Alexander Kromka[2]

[1]Department of Solid State Engineering, Faculty of Nuclear Sciences and Physical Engineering, Czech Technical University in Prague
[2]Department of Optical Materials, Institute of Physics, Czech Academy of Sciences
katerina.dragounova@fjfi.cvut.cz

Abstract

In this work, we performed study on behavior of silicon – vacancy center photoluminescence in diamond thin films prepared by microwave plasma enhanced CVD technique. Influence of substrate material (quartz, Al_2O_3, Mo and Si) on a reproducible fabrication of diamond thin films with Si-V optical centres is presented. Photoluminescence emission spectra were measured in the temperature range of 11 – 300 K. Activation energies for the thermal quenching of Si-V centre photoluminescence were determined and effect of substrate on photoluminescence properties is discussed too.

Keywords: Silicon-vacancy centre; Photoluminescence; CVD diamond.

Introduction

Silicon-vacancy centre (Si-V) is optical system formed by Si ions incorporated into diamond due to the etching of Si substrates, quartz windows or even bell jars of CVD reactor [1]. In diamond CVD films, the localised Si-V centres show spectrally narrow photoluminescence (PL) with the sharp zero phonon line (ZPL) at the vicinity of 738 nm accompanied by very weak phonon side band. Together with short lifetime of the excited state about 1 ns and high photostability, Si-V centres makes diamond a promising single-photon source [2]. Moreover, because the ZPL position falls into the transparency window of biological tissues in the near infrared spectral region, their luminescence is a suitable tool for bioimaging [2].

For diamond films and nanoparticles, many works were devoted to study of luminescence process activated by Si-V centres [3] and influence of deposition parameters on their PL activity as quality of substrate material [4], substrate temperature or composition of deposition gas [5]. Nevertheless, reproducible fabrication of luminescent diamond based material with controllable yield of Si-V centres PL is still a technological challenge.

In this paper, we present the correlation between the substrate material and the intensity of Si-V colour centres PL.

Experimental setup

Nanocrystalline diamond thin films were grown on quartz, Al_2O_3, molybdenum (Mo), and Si (100) substrates with size up to 10×10 mm^2 and thicknesses 1 mm, 1 mm, 0.6 mm, and 0.5 mm respectively. All NCD films were deposited together at the same process conditions in hydrogen rich plasma with methane (1% CH_4 with respect to H_2 flow). All deposition parameters are detaily introduced in [6]. Surface morphology was characterised by scanning electron microscopy (SEM, e_LiNE writer, Raith GmbH). Thickness of diamond films was measured by using reflectance interferometry and evaluated by commercial Film Wizard software (Scientific Computing International). The chemical composition and PL activity of Si-V centres in NCD

films were studied by Raman and PL spectroscopy at room temperature using a Renishaw In Via Reflex Raman spectrometer with CCD camera and 442 nm excitation wavelength.

Results and Discussion

Surface morphology of NCD films deposited on various substrate materials reveals well faceted grains with different average sizes and evaluated film thicknesses as well (for details, see reference [6]). All Raman spectra consist of the pronounced diamond peak centred near ~1331 cm^{-1} corresponding to good films quality. In PL spectra, emission from Si-V centres dominates also. For detailed discussion of Raman and PL spectra, see [6]. Figure 1 shows the ZPL integral intensity and the ratio of diamond/nondiamond carbon phase areas for various substrate materials. Although diamond/nondiamond phase ratios are almost comparable in NCD films deposited on Al_2O_3 and Si substrates, former demonstrates poor ZPL intensity, whereas the ZPL integral intensity in latter is several times higher. For NCD grown on a quartz substrate, the ratio of diamond/nondiamond is lower, but PL integral intensity reaches the maximum. With a further drop of the ratio, for the NCD film on molybdenum substrate, integral ZPL intensity decreases again.
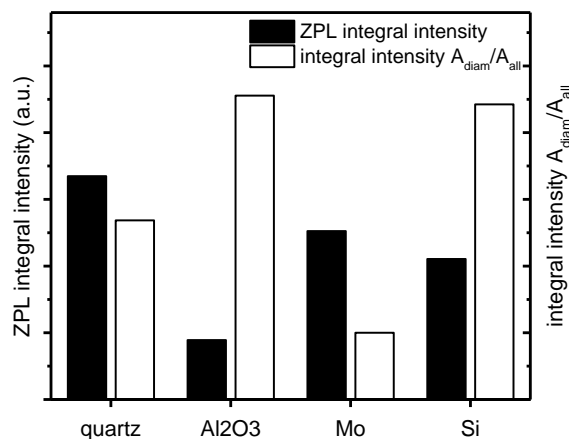
Figure 1: ZPL integral intensity (full bars) and the ratio of areas of Raman peaks corresponding to diamond and nondiamond phase (empty bars) in NCD films deposited on the various substrate material [6].

We explained results in Figure 1 in sense of influence of different sp^2 carbon phase ratio in our films. First, for intensive Si-V photoluminescence, certain ratio of non-diamond carbon phase is needed, as was shown in [5], it relates with the creation of silicon-vacancy pair. Second, sp^2 phase introduces continuum of states into the gap. Because Si-V centre PL is not excited resonantly in our case, these continuum might act as absorption centres collecting excitation energy, which is consecutively transferred to the Si-V centre. Thus, with increase of sp^2 phase content, rise in PL intensity should be expected due to increasing amount of excitation energy absorbed and transferred to Si-V centres. In Figure 1, the film on Al_2O_3 substrate has the highest diamond quality, thus the lowest density of absorbing centres and probably the lowest concentration of Si-V pairs. For film on Si substrate, similar quality was reached, but due to the Si-containing substrate one should assume higher concentration of Si-V centres. Maximal Si-V ZPL intensity for film on quartz should be result of the optimal amount of non-diamond carbon phase and concentration of Si-V centres, again supported by Si-containing substrate. In similar line of arguments, we assume that ZPL intensity obtained for film on Mo substrate is rather result of the highest amount of sp^2 phase.

Conclusion

Nanocrystalline diamond thin films grown on various substrates were analysed using steady-state photoluminescence, Raman scattering, and SEM measurements. Our results suggest that substrate material influenced the seeding and CVD film growth, and concentration of PL active Si-V centres within the film via etching of Si-containing substrates and ratio of non-diamond carbon phases. Non-diamond carbon phases ensure the presence of structural defects, acting as absorbing centres for PL excitation energy transfer.

References

[1] E. Neu, et al. Electronic transitions of single silicon vacancy centers in the near-infrared spectral region. *Phys Rev B* **85**(24): 245207-1–9, 2012.

[2] R. J. Narayan, et al. Medical applications of diamond particles & surfaces. *Mater Today* **14**(4): 154–163, 2011.

[3] K. Iakoubovskii, G. J. Adriaenssens. Optical detection of defect centers in CVD diamond. *Diam Relat Mater* **9**(7): 1349–1356, 2000.

[4] V. S. Sedov, et al. Gas-phase growth of silicon-doped luminescent diamond films and isolated nanocrystals. *Bull Lebedev Phys Inst* **38**(10): 291–296, 2011.

[5] Š. Potocký, et al.: Influence of gas chemistry on Si-V color centers in diamond films. *Phys Status Solidi B* **252**(11): 2580–2584, 2015.

[6] K. Dragounová, et al. Influence of substrate material on spectral properties and thermal quenching of photoluminescence of silicon vacancy colour centres in diamond thin films. *J Electr Eng-Elektrotechnický Časopis* **68**(7): 3–9, 2017.

Real Structure of Cold-Rolling Single and Two-Phase Steels

Jiří Čapek, Karel Trojan, Jakub Němeček, Nikolaj Ganev

Department of Solid State Engineering, Faculty of Nuclear Sciences and Physical Engineering, Czech Technical University in Prague

Abstract

The aim of this contribution was to compare the real structure of single-phase with two-phase steel after cold-rolling. Preferred orientation was studied as a function of sample thickness reduction. Type and also strength of determined preferred orientation depending on material and thickness reduction were studied. For analyses, X-ray diffraction were used.

Keywords: Ferritic steel; Duplex steel; Rolling; Texture; Fibres.

Introduction

Duplex stainless steels have high corrosion resistance in many environments, where the standard austenitic and ferritic steel is consumed, and where their properties significantly exceed single phase steel. Duplex steels combine properties of both phases and moreover, due to two-phase microstructure, some properties are better than high-alloyed single phase steel, e.g. abrasion resistance [1]. Thereby, smaller amount of material from duplex steel is necessary to manufacture function components. Duplex steels are due to austenite phase susceptible to mechanical reinforcement, i.e. local changes in mechanical properties of surface layers.

The importance of the texture resides in the anisotropy of most material properties. For this reason, the determination and subsequent interpretation of the texture in material engineering is very important. Moreover, texture analysis during the thermo-mechanical processing of materials provides information on basic mechanisms including deformation, recrystallization or phase transformation. The properties, which are influenced, are, for example, the Young's modulus of elasticity, Poisson number, hardness, strength, ductility, abrasion resistance, magnetic permeability, electrical conductivity etc. So called plastic anisotropy prefer to use a certain slide plane system during deformation. Texture is therefore used in the production of materials with specific properties [2]. Major deformation mechanisms responsible for the formation of ferrite and austenite rolling textures in duplex steels should be the same as in the single phase steels; however their contribution and significance are expected to change [3].

Theory and experiment

Generally, metals and alloys with a body centred cubic lattice (bcc) tend to form fibre textures. For bcc material, there are six characteristic fibres [4]. Most orientations are formed into two characteristic fibres of Euler space, determined by Euler angles in Bunge notation **g**. During cold rolling, primarily, the α_1 and γ fibre are created. The α_1 fibre is characterized by crystallographic direction *<110>* which is parallel to rolling direction, e.g. *{001}<110>, {112}<110>, {111}<110>*. The γ fibre include crystallographic directions with *{111}* planes which are parallel to normal direction, e.g. *{111}<110>, {111}<112>* [2, 3, 5]. The values of texture components are significantly dependent on the structure (especially on the grain size and initial texture), chemical and phase composition [3].

The tested samples of plate shape were made of AISI 420 (ferritic) and AISI 318LN (duplex) type of stainless steel. The samples were rolled with 0, 10, 20, 30, 40, and 50% reduction of

thickness. At the end, the samples were annealed in vacuum laboratory furnace for 7 hours at 650°C in order to reduce residual stresses.

Using Co*Kα* radiation, *X'Pert PRO MPD* diffractometer was used to sample analysis. Texture analysis was performed on the basis of the orientation distribution function (ODF) calculated from experimental pole figures recorded of three planes *{110}/{220}, {200},* and*{211}* using MTEX software.

Results and discussion

According to [3], after 40% of deformation the rolling texture of ferrite may be described by the limited *α₁, ε,* and *γ* fibres, see Figure 1a. It is evident that initial texture (0% deformation) is nearly random. For higher degree of deformation, *α₁* and *γ* fibres are dominant components of rolling texture of ferritic steel. Ferritic steel exhibited the *{001}<110>*, *{112}<110>*, and *{111}<110>* orientations which are components of *α₁* fibre texture. Rotated cubic orientation *{001}<110>* is one of the typical components of ferrite rolling texture. All fibres assume the higher values of the ODF or *f(g)* for increasing degree of deformation. Both fibres *α₁* and *ε* describing the final texture are very inhomogeneous.
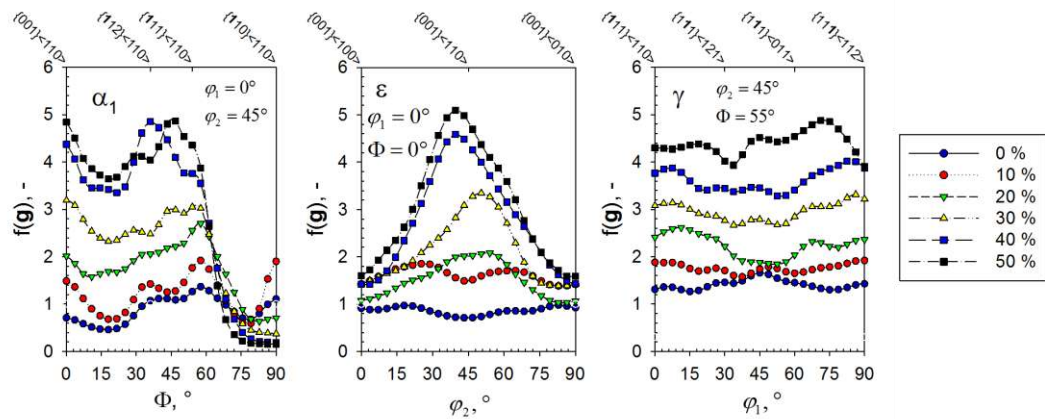
Figure 1a. Values of ODF along individual fibres (*α₁, ε,* and *γ*) of ferritic steel.
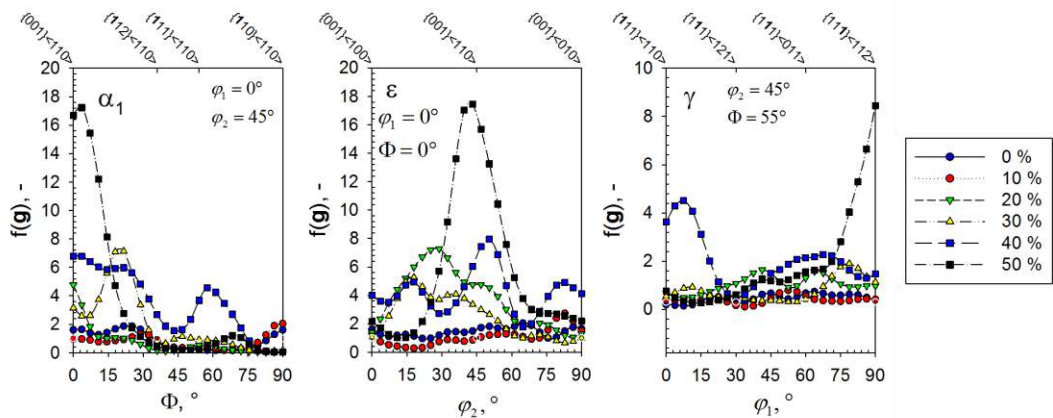
Figure 1b. Values of ODF along individual fibres (*α₁, ε,* and *γ*) of ferrite phase of duplex steel.

Nevertheless, it is necessary to expect that two-phase steel have different behaviour of the constituent phases in comparison with single-phase steel [6]. In most cases, there will be

differences between the textures of two- and single-phase steels. According to [3], these values of fibers are not typical for ferrite phase in duplex steels.

Despite of ferritic steel, ODFs of α phase of duplex steel are not consist of texture fibre, but only of the particular texture components. With increasing rolling reduction the significant increasing of the intensity was observed for the major component *{001}<110>* reaching intensity *f(g)* = 18. For 0–20% rolling reductions, the intensity of texture fibres/components are around value *f(g)* = 1.5, see Figure 1b. Moreover, after 30% of deformation, intensities of texture components *{112}<110>*, *{111}<110>*, and *{111}<112>* from the limited α_1-fiber and γ-fibre, respectively, are stronger.

Because of slip system of bcc materials, fibre-type texture develops in single-phase materials. Therefore, the typical texture components for single-phase steel are *{001}<110>*, *{112}<110>*, *{111}<110>*, and *{111}<112>*. These components are primarily part of the α_1 and γ fibre. However, in contrast to this, the dominant texture component is only *{001}<110>* for α phase of duplex steel.

Conclusions

The present study showed:
- The intensity and development of texture component are different for both types of steels.
- With increasing degree of deformation of ferritic sample, a considerable increasing the texture intensity was observed, from the value *f(g)* = 1 for the starting material to *f(g)* = 5 at 50% of rolling reduction.
- For ferritic sample, there are four main texture components *{001}<110>*, *{112}<110>*, *{111}<110>*, and *{111}<112>* which are parts of α_1, ε, and γ-fibre.
- For α phase of duplex steel, only rotated cube component *{001}<110>* is dominant.
- The texture for α phase of duplex steel is sharper compared to ferritic sample.

References

[1] R. Dakhlaoui, C. Braham, A. Baczmański. Mechanical properties of phases in austeno-ferritic duplex stainless steel-Surface stresses studied by X-ray diffraction. *Mater Sci Eng: A* **444**(1): 6–17, 2007.

[2] H. J. Bunge. *Texture Analysis in Materials Science.* Butterworth, London, 1982.

[3] J. Ryś, W. Ratuszek, M. Witkowska. Comparison of the Rolling Texture Formation in Duplex Steels with Various Initial Textures. *Arch Metall Mater* **51**(3): 495–502, 2006.

[4] S. Suwas, R. K. Ray. *Crystallographic Texture of Materials.* Springer-Verlag, 2014.

[5] H. Hu. Texture of metals. *Texture* **1**(4): 233–258, 1974.

[6] J. Čapek, K. Kolařík, Z. Pitrmuc, L. Beránek, N. Ganev. Residual Stress Determination of Duplex and Austenite Steels Machined using Different Tool Geometry. *Material Structure* **23**(4): 362–363, 2016.

Diffraction Study of Macroscopic Residual Stresses of Cutting Ceramics

Jakub Němeček, Jiří Čapek, Nikolaj Ganev, Kamil Kolařík

Department of Solid State Engineering, Faculty of Nuclear Sciences and Physical Engineering, Czech Technical University in Prague

Abstract

Currently, the extensive research in the field of cutting ceramics is conducted and there are efforts to replace cemented carbides by these materials. However, the problem is to improve the production of ideal compact samples. Therefore, the influence of mechanical machining technologies on the values of macroscopic residual stresses was investigated by X-ray diffraction. The resulting values were discussed depending on machining parameters and surface structure of the studied samples.

Keywords: Cutting ceramics; X-ray diffraction; Residual stress; Machining technology.

Introduction

A development of cutting ceramics has begun at the beginning of 20th century. Nowadays, there is an attempt to optimize the production process and machining parameters depending on the real structure of ceramic tiles [1]. In cooperation of Moscow State Technological University Stankin (MSTU Stankin), which provides preparation of samples, the macroscopic residual stresses were analysed by X-ray diffraction. Analysed samples were prepared from different materials such as trigonal Al_2O_3 (samples 2.x), hexagonal Si_3N_4 (samples 3.x), hexagonal SiC (samples 4.x), and tetragonal ZrO_2 (samples 5.x). They were finished with different mechanical surface treatments, specifically grinding by diamond disc (samples x.1–x.3) and air abrasive treatment (AAT, samples x.9–x.11).

Experiment

The influence of machining parameters on the surface values of macroscopic residual stresses was studied by X-ray diffraction. For grinding by diamond disc, the impact of transverse displacement on the lift F_d was studied, and for the AAT, where the sample rotated, the influence of loading time T was analysed. Values of residual stresses were determined in two orthogonal directions L (direction of grinding) and T (direction of transverse displacement).

Table 1: Parameters of grinding by diamond disc and AAT.

Sample	$F_d,$ [mm]	Sample	$T,$ [s]
x.1	0.5	x.9	15
x.2	1.0	x.10	30
x.3	1.5	x.11	60

Results and discussion

At first, all samples were machined by diamond disc and some of them subsequently machined by air abrasive treatment. Depending on the structure, various effects of machining technology on the surface structure were found (see Figure 1).
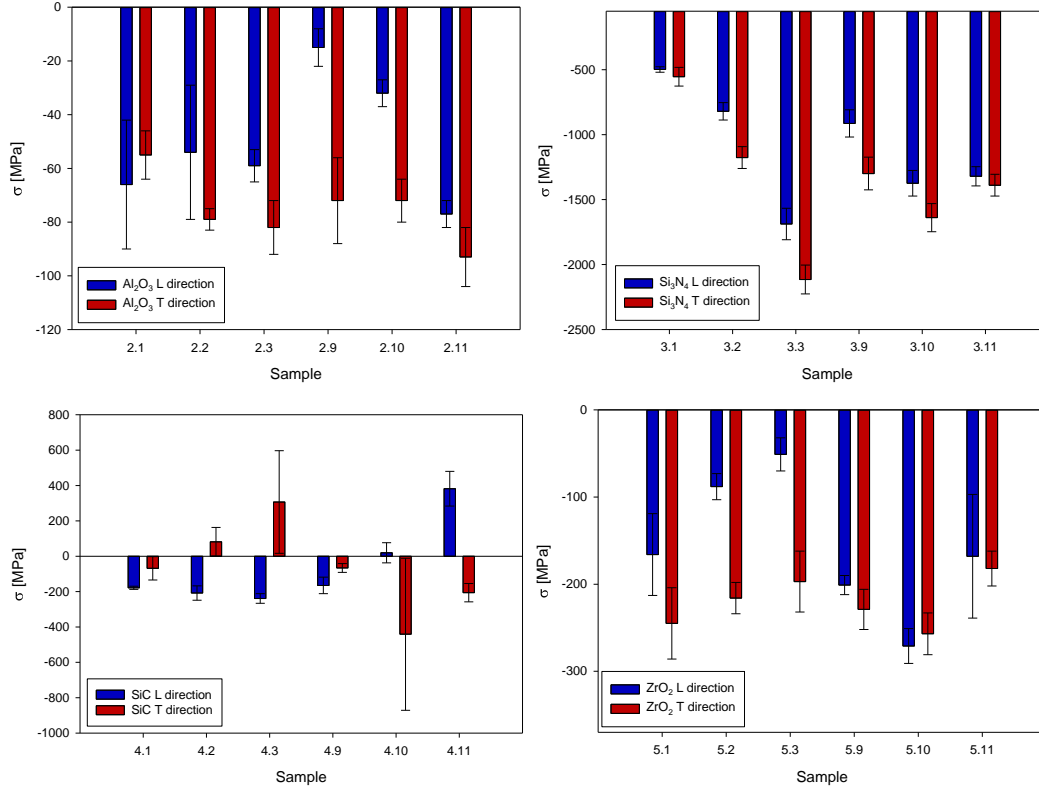

Figure 1: Values of macroscopic residual stresses after grinding by diamond disc (samples x.1–x.3) and AAT (samples x.9–x.11) of Al_2O_3, Si_3N_4, SiC and ZrO_2 in two mutually perpendicular directions.

For trigonal Al_2O_3, the values of residual stresses have expecting character, i.e. while after grinding by diamond disc in direction L, values of compressive residual stresses decrease with increasing F_d, in direction T, the compressive residual stresses increase. For AAT, an isotropy of residual stresses increase with increasing time of loading and the values of compressive residual stresses decrease at the same time.

In the case of Si_3N_4, the residual stresses were analysed by different experimental geometry due to overlap of diffraction lines with diffraction angles above 110° 2θ. It means the resulting values of residual stresses are from thinner surface (ca. 4x thinner). An accuracy of determination of position 2θ is about 8.5× smaller than for diffraction lines with higher angles 2θ. However, the relative dependence for determining the effect of mechanical machining on surface residual stresses is indicative. After diamond wheel grinding, we see a growth of compressive stresses in the both directions with increasing F_d. This is caused by hexagonal close packed structure of Si_3N_4 and its resistance to machining. As it has been shown in [2], machining materials with the hexagonal close packed lattice can cause an increase in compressive residual stresses in the direction of grinding. This effect is induced by the reaction of the structure to a force effect which resists plastic deformation.

After air abrasive treatment of Si_3N_4 samples, we see the effect of the previous machining technology. At a short machining time, the macroscopic residual stresses have a relatively large

anisotropy and, with increasing machining time, this anisotropy disappears. At the same time, it can be seen that with the machining time the values of the surface compressive residual stresses increase, which is again caused by the hexagonal structure. Compressive stresses dropped for sample 3.11 probably by sliding along the grain boundaries (there was an increase in crystallite size, see [3]).

For hexagonal SiC, it can be seen that in case of grinding with a diamond disc in the direction of grinding (direction L), the values of the compressive residual stresses increase and in the direction perpendicular (direction T), the tensile residual stresses decrease. This dependence is inconsistent with expectations, since in general grinding causes tensile stresses in the direction of grinding and in the perpendicular direction the compressive residual stresses. It is caused again by hexagonal close packed structure of SiC, see [2].

Values of macroscopic residual stresses after air abrasive treatment of SiC samples show very high experimental errors. These are due to the large dimensions of crystallites. However, it is evident that in the L direction, the values of the compressive residual stresses decrease, even tensile stresses increase, and in the T direction the compressive stresses on the contrary increase. This is caused again by the influence of the hexagonal lattice and its resistance to plastic deformation.

After grinding by diamond disc of ZrO_2, it is evident that the values of the compressive macroscopic residual stresses decrease with the increasing F_d. This is due to the thermal overload of the surface. The thermal conductivity coefficient for ZrO_2 is approximately one-tenth compared to other studied materials ($\lambda = 2.7\ \mathrm{Wm^{-1}K^{-1}}$ for ZrO_2, other ceramics have a temperature coefficient $\lambda = 30\ \mathrm{Wm^{-1}K^{-1}}$ and more).

For air abrasive treatment, it is obvious that due to the rotational movement of the ZrO_2 samples, an isotropic distribution of macroscopic residual stresses has occurred, the values in the L and T directions are same within the error.

Conclusions

An analysis of macroscopic residual stresses of surfaces of 4 different ceramic materials was performed by X-ray diffraction and the effect of mechanical machining on the surface structure was determined. Different reactions of hexagonal structures on mechanical machining were observed. It was found that ZrO_2 due to poor thermal conductivity had to be machined at lower speeds or pressures, otherwise the heat load of the structure would increase and the tensile residual stresses would increase.

References

[1] A. Humár. *Materiály pro řezné nástroje*. MM publishing, Praha, 2008.
[2] K. T. Ramesh. Effects of high rates of loading on the deformation behavior and failure mechanisms of hexagonal close-packed metals and alloys. *Metall Mater Trans* **33**(3): 927–935, 2002.
[3] J. Němeček, *Diffraction study of selected characteristic of cutting ceramics*, diploma thesis, FNSPE CTU in Prague, 2017.

Effect of Annealing on the Microstructure of Advanced Laser Processed AISI H13 Tool Steel

Karel Trojan[1], Václav Ocelík[2], Nikolaj Ganev[1], Stanislav Němeček[3], Jiří Čapek[1]

[1]CTU in Prague, Department of Solid State Engineering, Faculty of Nuclear Sciences and Physical Engineering, Trojanova 13, 120 00 Prague 2, Czech Republic
[2]Department of Applied Physics, Zernike Institute for Advanced Materials, Faculty of Science and Engineering, University of Groningen, Nijenborgh 4, 9747 AG, Groningen, The Netherlands
[3]RAPTECH s. r. o., U Vodárny 473, 330 08 Zruč-Senec, Czech Republic
karel.trojan@fjfi.cvut.cz

Abstract

The aim of this paper is to describe the effects of annealing on the microstructure of laser clad AISI H13 tool steel. This technology has the potential to replace conventional methods to repair dies. Subsequently, the problem of indexing of Kikuchi bands during the evaluation electron backscatter diffraction data and their mutual comparison is outlined.

Keywords: Laser processing; Cladding; Annealing; Microstructure; AISI H13 tool steel.

Introduction

Hot working tool steel AISI H13 is one of the most common die material used in metal and casting industries. Dies suffer damage due to wear and thermo-dynamic stresses during their lifetime [1]. Therefore, various methods have been developed for its repair. A great benefit of laser cladding in this field is a high productivity with minimal influence on surrounding material by thermal stresses [2]. Therefore, the aim of this contribution is to describe the effects of annealing on the microstructure of laser cladded AISI H13 tool steel using orientation imaging microscopy (OIM) which is using electron backscatter diffraction (EBSD) and energy-dispersive X-ray spectroscopy (EDS). During the laser cladding, rapid cooling and thus the formation of brittle martensitic microstructure could occur [3]. Hence, it is important to observe the effect of annealing on the microstructure which subsequently influences the properties of the newly created surface of dies.

Experimental

Laser cladding was carried using a diode laser *Laserline* 5.5 kW with optical head *Precitec Y52*. Laser power density 140 J/mm^2 was applied to form a single clad with the length of 137 mm, width of 6 mm and height of approx. 1 mm above substrate. The first sample from the clad was analysed without heat treatment. The second sample was annealed at 550 °C for 2 hours and the third sample was treated twice for two hours.

The OIM data was collected using a *Philips XL 30 FEG* scanning electron microscope equipped with a *TSL OIM system* based on *DigiView 3* camera and *EDS EDAX SUTW+* detector. The accelerating voltage of 15 kV and 50 nm step size of scanning were used. A grain boundary is defined in the microstructure as a boundary between two neighbouring scanning points having crystallographic misorientation larger than 5°. All EBSD data were analysed with *TSL OIM Analysis 7.3.0* software and only data points with *Confident index* higher than 0.05 were used. *Confident index* is based on voting scheme during automated indexing of

the diffraction pattern where it is counted as a ratio of votes for the best solution minus votes for the second best solution divided by total possible number of votes from the detected Kikuchi bands. Certain crystallographic orientation receives a vote when observed angles between the three bands are the same as table values of given orientation. *Confident index* 0.05 corresponds on a face-centred cubic material to approx. 70% probability of correct indexing.

Results and discussion

Table 1 gives the range of the chemical composition of H13 steel determined by ISO 4957 [4], the next row shows average chemical composition and standard deviation obtained by EDS on a cross-section of four randomly selected particles of the used powder; the bottom row shows the average chemical composition and standard deviation in four different clad cross-section areas of dimensions approx. 500×250 μm^2. In the clad, chromium is on average about one weight percentage less than prescribed standard, see Table 1.

Table 1: Chemical composition of the steel AISI H13 according to ISO 4957 [4], the powder and the clad.

	Cr [Wt.%]	Mo [Wt.%]	Si [Wt.%]	V [Wt.%]	Mn [Wt.%]	C [Wt.%]
EN ISO 4957	4.80–5.50	1.20–1.50	0.80–1.20	0.85–1.15	0.25–0.50	0.35–0.42
Powder H13	5.10 ± 0.07	1.79 ± 0.08	0.92 ± 0.11	1.08 ± 0.02	0.45 ± 0.07	
Clad	3.77 ± 0.05	1.21 ± 0.05	0.72 ± 0.01	0.84 ± 0.03	0.62 ± 0.03	

Figure 1 graphically illustrates the effect of annealing on the microstructure of the weld. Three samples were used, so the measured area was not the same. As shown also in Figure 2, it can be stated that the annealing time increases the proportion of carbides and decreases the austenite fraction. This effect is well known and not surprising when diffusion is facilitated by higher temperature. However, the weight percentage of the carbides that were indexed during the measurement is inconsistent with Table 1. Carbides have been indexed three times more than the steel composition obtained by EDS analysis showed.

Inverse pole figures of ferrite in the selected area before and after annealing are shown in Figure 3, where in individual colours correspond to the normal vectors of crystallographic planes that are parallel to the normal vector of the cross-section of the sample. After cladding, the martensitic structure could be observed and vice versa after annealing. However, a slight rounding of corners of martensitic laths can be found after annealing for 2+2 hours.
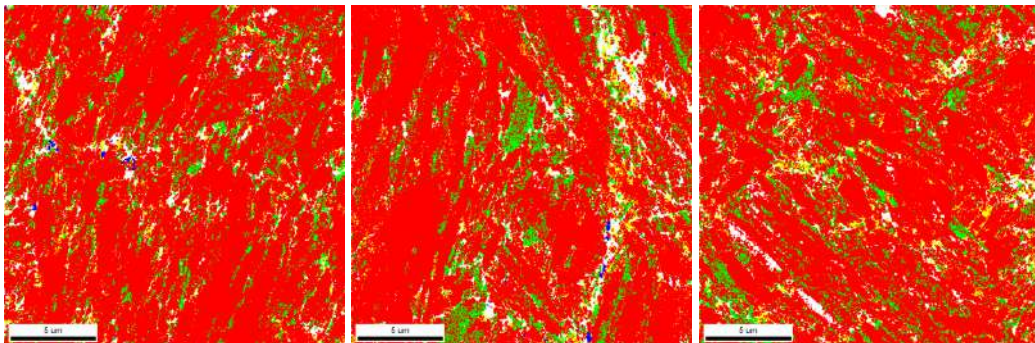
Figure 1: Effect of annealing on the phase composition of the clad where ferrite is red, $Cr_{23}C_6$ green, VC yellow and austenite blue (left as cladded, middle 550 °C for 2 h, right 550 °C for 2+2 h).
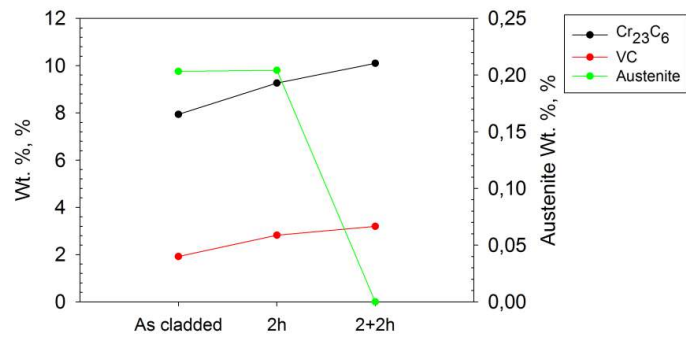
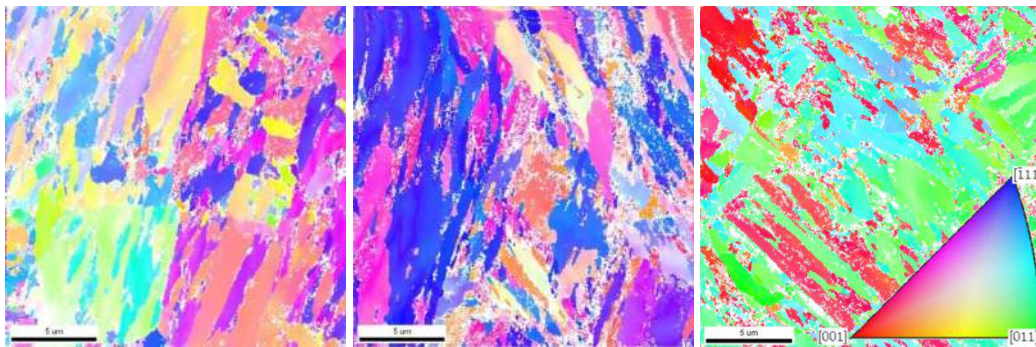Figure 3: Effect of annealing on the microstructure of the clad.

Figure 4: Effect of annealing on the microstructure of the ferrite of the clad (left as cladded, middle 550 °C for 2 h, right 550 °C for 2+2 h).

Conclusions

Laser deposition of the H13 tool steel showed a great application potential. The research topic and primarily the difference between EDS and EBSD has not yet been accurately described and understood, so further measurements and adjustments of the indexing parameters will be needed. Based on these results, annealing is not needed after cladding. However, further measurements are required, in particular hardness and wear resistance.

References

[1] R. G. Telasang, et al. Microstructure and Mechanical Properties of Laser Clad and Post-cladding Tempered AISI H13 Tool Steel. *Metall Mater Trans A* **46A**: 2309–2321, 2015.
[2] M. Vedani, et al. Problems in laser repair-welding a surface-treated tool steel. *Surf Coat Tech* **201**: 4518–4525, 2007.
[3] J. Chen, et al. On the development of microstructures and residual stresses during laser cladding and post-heat treatments. *J Mater Sci* **47**(2): 779–792, 2012.
[4] ISO 4957:1999. *Tool steel*. 2nd. International Organization for Standardization, 2009.

Program

	Pondělí 18.9.	Úterý 19.9.	Středa 20.9.	Čtvrtek 21.9.	Pátek 22.9.
08:00		Snídaně	Snídaně	Snídaně	Snídaně
09:00		Tyc (Karlík)	Vilémová	Kopecký (Heczko)	Hájek (Neugebauer)
09:20		Štefan	Veverka	Veřtát	Dragounová
09:40		Ondráček	Tesař	Drahokoupil	Zajac
10:00		Čech		Dudr	
10:20		Coffe break	Coffe break	Coffe break	Coffe break
10:40		Karlík (Landa)	Kraus 10:20 – 11:20 (Kalvoda)	Stráník (Sedlák)	Kučeráková (Stráník)
11:00					Čapek
11:10		Aubrecht		Neugebauer	
		Koubský			Němeček
11:40			Oběd		Trojan
12:00		Oběd		Oběd	Závěr Kalvoda
			Atomové muzeum - prohlídka/ výlet		
14:00		Landa (Kalvoda)		Heczko (Kalvoda)	Oběd
14:30		Levinský		Koller	
14:50		Coffe break		Coffee break	
15:10		Fojtíková (Aubrecht)		Kolenko (Drahokoupil)	
15:30		Sedlák		Švecová	
15:50		Dráb		Malý	
16:00	Úvod Kalvoda				
16:20	Hejtmánek (Kalvoda)				
16:50	Skočdopole				
17:10	Kalvoda				
19:00	Večeře	Večeře	Večeře	Večeře	

Jméno v závorce je chairman
Malá prezentace: 20 minut (15min + 5 min diskuze)
Velká prezentace: 30 minut (25min + 5 min diskuze)

Obsah